1

2 Ocean biogeochemistry in the Canadian Earth System Model version 5.0.3: CanESM5 and
3 CanESM5-CanOE

4

5 James R. Christian[1,2], Kenneth L. Denman[2,3], Hakase Hayashida[3,4], Amber M. Holdsworth[1],
6 Warren G. Lee[2], Olivier G.J. Riche[3,5], Andrew E. Shao[2,3], Nadja Steiner[1,2], and Neil C. Swart[2]

7

8 1 Fisheries and Oceans Canada, Sidney, BC, Canada
9 2 Canadian Centre for Climate Modelling and Analysis, Victoria, BC, Canada
10 3 School of Earth and Ocean Sciences, University of Victoria, Victoria, BC, Canada
11 4 now at the Institute for Marine and Antarctic Studies, University of Tasmania, Hobart,
12 Tasmania, Australia
13 5 now at Fisheries and Oceans Canada, Mont Joli, Québec, Canada

14

15

16 *Correspondence to*: James Christian (jim.christian@ec.gc.ca)

17

18

19   **Abstract.** The ocean biogeochemistry components of the Canadian Earth System Model v. 5 are

20   presented and compared to observations and other models. CanESM5 employs the same

21   biogeochemistry module as CanESM2 whereas CanESM5-CanOE ("Canadian Ocean Ecosystem

22   model") is a new, more complex biogeochemistry module developed for CMIP6, with multiple

23   food chains, flexible phytoplankton elemental ratios, and a prognostic iron cycle. This new

24   model is described in detail and the outputs compared to CanESM5 and CanESM2, as well as to

25   observations and other CMIP6 models. Both CanESM5 models show gains in skill relative to

26   CanESM2, which are attributed primarily to improvements in ocean circulation. CanESM5-

27   CanOE shows improved skill relative to CanESM5 in some areas. CanESM5-CanOE includes a

28   prognostic iron cycle, and maintains high nutrient / low chlorophyll conditions in the expected

29   regions (in CanESM2 and CanESM5, iron limitation is specified as a temporally static 'mask').

30   Surface nitrate concentrations are biased low in the subarctic Pacific and equatorial Pacific, and

31   high in the Southern Ocean. Export production in CanESM5-CanOE is among the lowest for

32   CMIP6 models; in CanESM5 it is among the highest, but shows the most rapid decline after

33   about 1980. CanESM5-CanOE has relatively low concentrations of zooplankton and detritus

34   relative to phytoplankton, and a high and relatively constant living phytoplankton fraction of

35   total particulate organic matter. In most regions, large and small phytoplankton show decoupled

36   seasonal cycles with greater abundance of large phytoplankton in the productive seasons.

37   Cumulative ocean uptake of anthropogenic carbon dioxide through 2014 is lower in both

38   CanESM5 models than in observation-based estimates or the model ensemble mean, and is lower

39   in CanESM5-CanOE (122 PgC) than in CanESM5 (132 PgC).

40

Geoscientific
Model Development
Discussions

41   1. **Introduction**

42

43   The Canadian Centre for Climate Modelling and Analysis has been developing coupled models

44   with an interactive carbon cycle for more than a decade (Arora et al., 2009; 2011; Christian et al.,

45   2010). CanESM5 (Swart et al., 2019a) is an updated version of CanESM2 (Arora et al., 2011),

46   with an entirely new ocean and an atmosphere with the same T63 horizontal resolution and

47   important improvements in atmospheric physics. The CanESM5 ocean is based on the Nucleus

48   for European Modelling of the Ocean (NEMO) system version 3.4. The ocean biogeochemistry

49   modules were developed in-house, although parameterizations for some processes were adapted

50   from the native PISCES biogeochemistry model (Aumont et al., 2015). CanESM5 uses the same

51   biogeochemistry model as CanESM1 and CanESM2, the Canadian Model of Ocean Carbon

52   (CMOC; Zahariev et al., 2008), adapted for use within NEMO. An additional model was

53   developed for CMIP6, called the Canadian Ocean Ecosystem model (CanOE). The biological

54   components of CanOE are of substantially greater complexity, including multiple food chains,

55   flexible phytoplankton elemental ratios, and a prognostic iron (Fe) cycle. Carbon chemistry, gas

56   exchange and solubility of carbon dioxide (CO_2) and oxygen are identical between the two and

57   follow the protocols specified by the Ocean Model Intercomparison Project - Biogeochemistry

58   (OMIP-BGC) (Orr et al., 2017). The two coupled models are known as CanESM5 and

59   CanESM5-CanOE, respectively. There are no feedbacks between biology and the physical ocean

60   model, so the physical climate of CanESM5 and CanESM5-CanOE is identical in experiments

61   with prescribed atmospheric CO_2 concentration.

62

63   The reasons for developing both models are, firstly, to evaluate the effect of changes in ocean

64   circulation between CanESM2 and CanESM5 on ocean biogeochemistry by running the new

65   climate model with the same ocean biogeochemistry, and secondly because CanOE is

66   substantially more expensive computationally (19 tracers vs 7). Having CMOC as an option

67   allowed us to run many CMIP6 experiments with CanESM5 only, as ocean biogeochemistry is

68   not central to their purpose. Many additional tracers requested by OMIP-BGC including abiotic

69   and natural dissolved inorganic carbon (DIC), $DI^{14}C$, CFCs and SF_6 (see Orr et al.,2017) were

70   run only in CanESM5, since adding these tracers on top of the larger set of biological

71   components in CanOE would have been prohibitively expensive. The CMIP6 experiments

72   published for CanESM5-CanOE are listed in Supplementary Table S1.

73

74   CMOC is a nutrient-phytoplankton-zooplankton-detritus (NPZD) model with highly

75   parameterized representations of phytoplankton Fe limitation, dinitrogen (N_2) fixation and

76   denitrification, and calcification and calcite dissolution (Zahariev et al., 2008). In CanESM1 and

77   CanESM2, CMOC did not include oxygen. In CanESM5, CMOC now includes oxygen as a

78   purely 'downstream' tracer that does not affect other biogeochemical processes, whereas in

79   CanOE denitrification is prognostic and dependent on the concentration of oxygen. Among the

80   less satisfactory aspects of CMOC biogeochemistry are, firstly, that Fe limitation is specified as a

81   static 'mask' that does not change with climate (being calculated from the present-day

82   climatological distribution of nitrate), and secondly, that denitrification is parameterized so that

83   nitrogen (N) is conserved within each vertical column, i.e., collocated with N_2 fixation in tropical

84   and subtropical open-ocean regions (Zahariev et al., 2008; Riche and Christian, 2018). This latter

85   simplification produced excessive accumulations of nitrate in Eastern Boundary Current regions

86   where most denitrification actually occurs. CMOC also has a tendency to produce rather stark

87   extremes of high and low primary and export production (Zahariev et al., 2008), a well-known

88   problem of NPZD models (Armstrong, 1994; Friedrichs et al., 2007). Our intent in developing

89   CanOE was to alleviate, or at least reduce, these biases, by including multiple food chains, a

90   prognostic Fe cycle, and prognostic denitrification. Dinitrogen fixation is still parameterized, but

91   the CanOE parameterization includes Fe limitation, whereas in CMOC N_2 fixation tends to grow

92   without bound in a warming ocean as there is no P or Fe limitation (Riche and Christian, 2018).

93   Calcification is represented by a prognostic detrital calcite pool with its own sinking rate (distinct

94   from that of organic detritus), and calcite burial depends on the saturation state. In CMOC

95   calcification is parameterized by a temperature dependent "rain ratio" and 100% burial of calcite

96   that reaches the seafloor is assumed.

97

98   In this paper we present a detailed model description for CanOE and an evaluation of both

99   CanESM5 and CanESM5-CanOE relative to observational data products and other available

100   models. CMOC has been well described previously (Zahariev et al., 2008) and the details are not

101   reiterated here. In some cases, CanESM2 results are also shown to illustrate which differences in

102   the model solutions arise largely from the evolution of the physical ocean model, and which are

103   specifically associated with different representations of biogeochemistry.

104

105   **2. Model Description**

106

107   The NEMO system is a publicly available archive of codes based on the OPA (Océan

108   PArallelisé) ocean model (Madec and Imbard, 1996; Guilyardi and Madec, 1997). It comes with

109   two options for biogeochemistry: PISCES (Pelagic Interactions Scheme for Carbon and

110 Ecosystem Studies) and LOBSTER (LODyC Ocean Biogeochemical System for Ecosystem and

111 Resources). CanOE and the NEMO implementation of CMOC are built around the basic code

112 structure of PISCES within the Tracers in Ocean Paradigm (TOP) module, using NEMO v3.4.1,

113 but have also been implemented in NEMO 3.6 for regional downscaling applications

114 (Holdsworth et al., 2021).

115

116 The biology, carbon chemistry, gas exchange and light attenuation components have all been

117 modified to various degrees. In a few cases PISCES parameterizations, or slightly modified

118 versions thereof, were adopted. CanOE uses PISCES three-band light attenuation while NEMO-

119 CMOC uses broadband attenuation of photosynthetically active radiation (PAR) for consistency

120 with the published version of CMOC. Carbon chemistry was modified to be consistent with the

121 Best Practices Guide (Dickson et al., 2007) and the OMIP-BGC data request (Orr et al., 2017).

122 All calculations are done on the total scale and the recommended formulae for the equilibrium

123 constants are employed. The PISCES conventions for convergence of carbon chemistry

124 calculations were retained, the greater number of iterations in the surface layer offering greater

125 accuracy in calculating pCO_2 and gas exchange. In subsurface layers (where the only function of

126 the carbon chemistry is to calculate burial of calcite in the sediments) the number of iterations is

127 fixed at five. CanESM5 uses the same carbon chemistry but does not solve the carbon chemistry

128 equations in the subsurface layers.

129

130 The CanOE biology model is a substantially new model based on the cellular regulation model

131 of Geider et al. (1998). There are two phytoplankton functional groups, and each group has four

132 state variables: C, N, Fe and chlorophyll. Photosynthesis is decoupled from cell production and

6

133 photosynthetic rate is a function of the cell's internal N and Fe quotas. Each functional group has

134 a specified minimum and maximum N quota and Fe quota, and nutrient uptake ceases when the

135 maximal cell quota is reached. Chlorophyll synthesis is a function of N uptake and increases at

136 low irradiance. Model parameters and their values are listed in Table 1. A schematic of the

137 model is shown in Figure 1.

138

139 **2.1 Photosynthesis and Phytoplankton Growth**

140

141 For simplicity and clarity, the equations are shown here for a single phytoplankton species, and

142 do not differ structurally for small and large phytoplankton. Some parameter values differ for the

143 two phytoplankton groups; all parameter values are listed in Table 1.

144

145 Temperature dependence of photosynthetic activity is expressed by the Arrhenius equation

146 $$T_f = \exp(-\frac{E_{ap}}{R}(\frac{1}{T} - \frac{1}{T_{\text{ref}}}))$$ (1)

147 where E_{ap} is an enzyme activation energy that corresponds approximately to that of RuBisCo (cf.

148 Raven and Geider 1988), R is the gas constant (8.314 J mol^{-1} K^{-1}), and temperature T and

149 reference temperature T_{ref} are in Kelvin. Maximal rates of nutrient (either N or Fe, but

150 generically referred to here with the superscript X) uptake are given by

151 $$V_{max}^X = V_{ref}^X T_f (\frac{Q_{max}^X - Q^X}{Q_{max}^X - Q_{min}^X})^{0.05}$$ (2)

152 where $V_{max}{}^X$ is the maximal uptake rate in mg of nutrient X per mg of cell C, X can represent N

153 or Fe, Q is the nutrient cell quota and Q_{min} and Q_{max} its minimum and maximum values, and $V_{ref}{}^X$
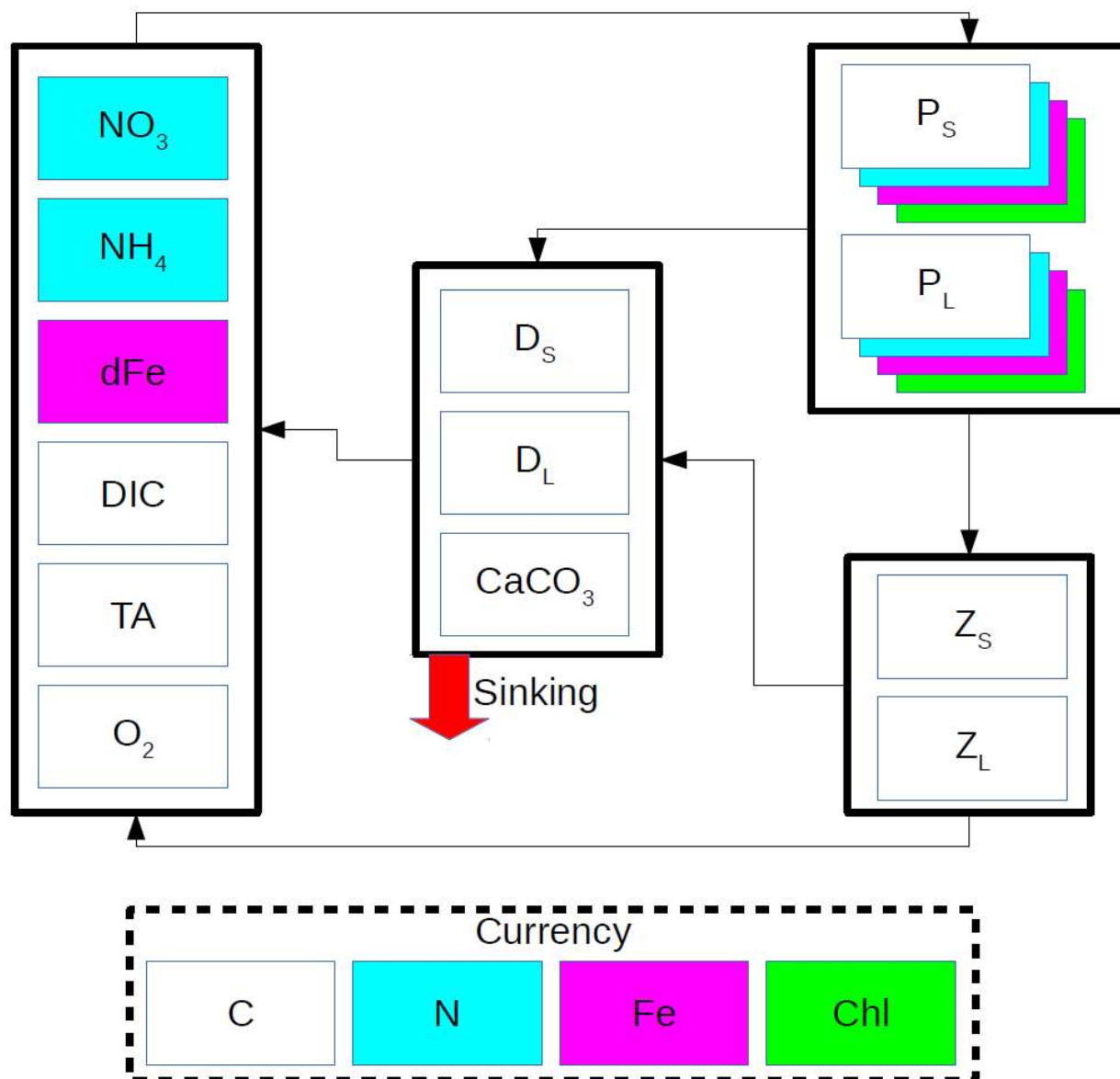
154

Figure 1 - Schematic of the CanOE biology model. Model currencies including chlorophyll (Chl) are indicated by coloured boxes except oxygen (O_2) and carbonate ($CaCO_3$). Arrows indicate flows of carbon (C), nitrogen (N) and iron (Fe) between compartments containing small (S) and large (L) phytoplankton (P), zooplankton (Z), and detritus (D) components; counterflows of oxygen are not shown.

Table 1 – Ecosystem model parameters.

Symbol	Description	Unit	
T_{ref}	Reference temperature	K	298.15
E_{ap}	Activation energy for photosynthesis	kJ mol^{-1}	37.4
Q^N_{mins}	Small phytoplankton minimum N quota	g N g C^{-1}	0.04
Q^N_{maxs}	Small phytoplankton maximum N quota	g N g C^{-1}	0.172
Q^N_{minl}	Large phytoplankton minimum N quota	g N g C^{-1}	0.04
Q^N_{maxl}	Large phytoplankton maximum N quota	g N g C^{-1}	0.172
Q^{Fe}_{mins}	Small phytoplankton minimum Fe quota	µg Fe g C^{-1}	4.65
Q^{Fe}_{maxs}	Small phytoplankton maximum Fe quota	µg Fe g C^{-1}	93.
Q^{Fe}_{minl}	Large phytoplankton minimum Fe quota	µg Fe g C^{-1}	6.5
Q^{Fe}_{maxl}	Large phytoplankton maximum Fe quota	µg Fe g C^{-1}	70.
V^N_{ref}	Reference rate of N uptake	g N g C^{-1} d^{-1}	0.6
V^{Fe}_{ref}	Reference rate of Fe uptake	µg Fe g C^{-1} d^{-1}	79.
P^C_{ref}	Reference rate of photosynthesis	g C g C^{-1} d^{-1}	3
k_{XU}	Rate coefficient for exhudation	d^{-1}	1.7
k_{dgr}	Rate coefficient for chlorophyll degradation	d^{-1}	0.02
ζ	Respiratory cost of biosynthesis	g C g N^{-1}	2
α_{chl}	Initial slope of P-E curve	g C g CHL^{-1} h^{-1} (µmol m^{-2} s^{-1})$^{-1}$	1.08
Θ_{max}^N	Maximum chlorophyll-nitrogen ratio	g g^{-1}	0.18
K_{NiS}	Half-saturation for small phytoplankton nitrate uptake	mmol^{-1} m^3	0.1
K_{NaS}	Half-saturation for small phytoplankton ammonium uptake	mmol^{-1} m^3	0.05
K_{FeS}	Half-saturation for small phytoplankton iron uptake	nmol^{-1} m^3	100
K_{NiL}	Half-saturation for large phytoplankton nitrate uptake	mmol^{-1} m^3	1.0
K_{NaL}	Half-saturation for large phytoplankton ammonium uptake	mmol^{-1} m^3	0.05
K_{FeL}	Half-saturation for large phytoplankton iron uptake	nmol^{-1} m^3	200
m_{1S}	Small phytoplankton/zooplankton mortality rate (linear)	d^{-1}	0.05
m_{2S}	Small phytoplankton/zooplankton mortality coefficient	(mmol C m^{-3})$^{-1}$ d^{-1}	0.06
m_{1L}	Large phytoplankton/zooplankton mortality rate (linear)	d^{-1}	0.1

m_{2L}	Large phytoplankton/zooplankton mortality coefficient	(mmol C m^{-3})$^{-1}$ d^{-1}	0.06
X_{minp}	Minimum phytoplankton concentration for linear mortality	mmol C m^{-3}	0.01
a_L	Large zooplankton grazing parameter	(mmol C m^{-3})$^{-1}$	0.25
G_{L0}	Large zooplankton maximum grazing rate	d^{-1}	0.85
a_S	Small zooplankton grazing parameter	(mmol C m^{-3})$^{-1}$	0.25
G_{S0}	Small zooplankton maximum grazing rate	d^{-1}	1.7
λ	Assimilation efficiency	n.d.	0.8
r_{zs}	Microzooplankton specific respiration rate at T_{ref}	d^{-1}	0.3
r_{zl}	Mesozooplankton specific respiration rate at T_{ref}	d^{-1}	0.1
r_1	Small detritus remineralization rate at T_{ref}	d^{-1}	0.25
r_2	Large detritus remineralization rate at T_{ref}	d^{-1}	0.25
E_{ar}	Activation energy for detritus remineralization	kJ mol^{-1}	54.0
w_s	Small detritus sinking speed	m d^{-1}	2.
w_l	Large detritus sinking speed	m d^{-1}	30.
w_{Ca}	CaCO$_3$ sinking speed	m d^{-1}	20.
P_{Ca}	CaCO$_3$ production as fraction of mortality	mol CaCO$_3$ molC^{-1}	0.05
k_{Ca}	CaCO$_3$ dissolution rate	d^{-1}	0.0074
S_{Fe1}	Dissolved iron scavenging loss rate (Fe$\leq$L$_{Fe}$)	d^{-1}	0.001
S_{Fe2}	Dissolved iron scavenging loss rate (Fe>L$_{Fe}$)	d^{-1}	2.5
L_{Fe}	Ligand concentration	nmol Fe m^{-3}	600.
P_{Fe}	POC-dependence parameter for Fe scavenging	(mmolC m^{-3})$^{-1}$	0.66
K_{NH4ox}	Nitrification rate in darkness	d^{-1}	0.05
K_E	Half-saturation for irradiance inhibition of nitrification	W m^{-2}	1.
k_{dnf}	Light and nutrient saturated rate of N$_2$ fixation at 30°C	mmol m^{-3} d^{-1}	0.0225
a	Initial slope for irradiance-dependence of N$_2$ fixation	(W m^{-2})$^{-1}$	0.02
K_{Fe}	Half-saturation for Fe dependence of N$_2$ fixation	nmol m^{-3}	100.
K_{NO3}	Half-saturation for DIN inhibition of N$_2$ fixation	mmol m^{-3}	0.1
O_{mxd}	O$_2$ concentration threshold for denitrification	mmol m^{-3}	6.
A_f	Anammox fraction of N loss to denitrification	n.d.	0.25

158   is a (specified) basal rate at $T=T_{ref}$ and $Q=Q_{min}$. These maximum rates are then reduced according

159   to the ambient nutrient concentration, i.e.

160    $$V^N = V_{max}^N(L_{NH4} + (1 - L_{NH4})L_{NO3})$$ (3a)

161   where $L_{\mathrm{NH4}} = \frac{N_a}{K_{\mathrm{NaX}}+N_a}$ and $L_{\mathrm{NO3}} = \frac{N_i}{K_{\mathrm{NiX}}+N_i}$, with N_i and N_a indicating nitrate and ammonium

162   respectively, and

163    $$V^{Fe} = V_{max}^{Fe} \left(\frac{\mathrm{Fe}}{K_{\mathrm{FeX}}+\mathrm{Fe}}\right)$$ (3b)

164   where X indicates large or small phytoplankton (Table 1). The maximal carbon-based growth

165   rate is given by

166    $$P_{max}^C = P_{ref}^C T_f \min\{\frac{Q^N-Q_{min}^N}{Q_{max}^N-Q_{min}^N} \cdot \frac{Q^{Fe}-Q_{min}^{Fe}}{Q_{max}^{Fe}-Q_{min}^{Fe}}\}$$ (4)

167   where P^C_{ref} is the rate at the reference temperature T_{ref} under nutrient-replete conditions

168    $(Q=Q_{max})$. The light-limited growth rate is then given by

169    $$P_{phot}^C = P_{max}^C \left(1 - e^{-\alpha_{chl}E\theta_C / P_{max}^C}\right)$$ (5)

170   where θ_C is the chlorophyll-to-carbon ratio. The rate of chlorophyll synthesis is

171    $$\rho_{\mathrm{chl}} = \theta_{max}^N \frac{P_{phot}^C}{E\alpha_{\mathrm{chl}}\theta}$$ (6)

172   These rates are then used to define a set of state equations for phytoplankton carbon (C_p),

173   nitrogen (N_P), iron (Fe_p), and chlorophyll (M).

174    $$\frac{\mathrm{d}C_p}{\mathrm{dt}} = (P_{phot}^C - \zeta V_N)C_p - (G + C_{\mathrm{XS}}) - m_1 C_p - m_2 C_p^2 - k_{\mathrm{XU}}C_{\mathrm{INTR}}$$ (7)

175   where ζ is the respiratory cost of biosynthesis, G is the grazing rate (equation 12), C_{XS} is the

176   excess (above the ratio in grazer biomass) carbon in grazing losses, m_1 and m_2 are coefficients

177   for linear and quadratic nonspecific mortality terms, C_{INTR} is the concentration of intracellular

178   carbohydrate carbon in excess of biosynthetic requirements, and k_{XU} is a rate coefficient for its

179   exudation to the environment. The nonspecific mortality terms are set to 0 below 0.01 mmol C

180   m^{-3}, to prevent biomass from being driven to excessively low levels in the high latitudes in

181   winter (Hayashida, 2018). The full equation for phytoplankton N, Fe and chlorophyll are

182
$$\frac{\mathrm{d}N_p}{\mathrm{d}t} = \frac{V^N}{Q_N} - (G + m_1 C_p + m_2 C_p^2)R_{\mathrm{NC}} - N_{\mathrm{XS}} \tag{8}$$

183
$$\frac{\mathrm{d}Fe_p}{\mathrm{d}t} = \frac{V^{\mathrm{Fe}}}{Q_{\mathrm{Fe}}} - (G + m_1 C_P + m_2 C_p^2)R_{\mathrm{FeC}} - Fe_{\mathrm{XS}} \tag{9}$$

184
$$\frac{\mathrm{d}M}{\mathrm{d}t} = \frac{\rho_{\mathrm{chl}} V^N}{\theta_C}M - (G + m_1 C_p + m_2 C_p^2)\theta_C - k_{\mathrm{dgr}}M \tag{10}$$

185   where k_{dgr} is a rate coefficient for nonspecific losses of chlorophyll e.g., by photooxidation, in

186   addition to losses to grazing and other processes that also affect C_p, N_p, and Fe_p. N_{XS} and Fe_{XS} are

187   remineralization of "excess" (relative to grazer or detritus ratios) N or Fe and are defined below

188   (equation 16).

189

190   **2.2 Grazing and Food Web Interactions**

191

192   Grazing rate depends on the phytoplankton carbon concentration, which most closely represents

193   the food concentration available to the grazer (Elser and Urabe 1999; Loladze et al. 2000).

194   Zooplankton biomass is also in carbon units. State equations for small and large zooplankton are

195
$$\frac{\mathrm{d}Z_s}{\mathrm{d}t} = \lambda G_s - (R + G_Z + m_{1s}Z_s + m_{2s}Z_s^2) \tag{11a}$$

196
$$\frac{dZ_L}{dt} = \lambda G_L - (R + m_{1L}Z_L + m_{2L}Z_L^2) \tag{11b}$$

197   where

198 $\quad G_s = G_{\text{so}}(1 - e^{-a_s C_{\text{ps}}})Z_s$ (12a)

199 $\quad G_L = G_{\text{L0}}(1 - e^{-a_l(C_{\text{pl}}+Z_s)})Z_L$ (12b)

200 for small and large zooplankton respectively, G_Z is grazing of small zooplankton by large

201 zooplankton, R is respiration, and m_1 and m_2 are nongrazing mortality rates. Large zooplankton

202 grazing is divided into grazing on large phytoplankton and small zooplankton in proportion to

203 the relative abundance of each

204 $\quad G_P = G_L \frac{P_l}{P_l+Z_s}$ (13a)

205 $\quad G_Z = G_{lL} \frac{Z_s}{P_l+Z_s}$ (13b)

206 Zooplankton biomass loss to respiration is given by

207 $\quad R = max\{r_z T_f Z - C_{\text{XS}}. 0\}$ (14)

208 and uses the same activation energy as photosynthesis. Respiration (R) is assumed to consume

209 only carbon and not result in catabolism of existing biomass when "excess" carbon is available

210 in the prey. In addition, conservation of mass must be maintained by recycling to the dissolved

211 pool grazer consumption of elements in excess of biosynthetic requirements when grazer and

212 prey elemental ratios differ. In the case where the nutrient quota (relative to carbon) exceeds the

213 grazer fixed ratio, the excess nutrient is remineralized to the dissolved inorganic pool. In the case

214 where the nutrient quota is less than the grazer ratio, the grazer intake is reduced to what can be

215 supported by the least abundant nutrient (relative to the grazer biomass ratio) and excess carbon

216 is remineralized. For the case of two nutrients (in this case N and Fe) it is necessary to define

217 $\quad G' = G \min\left\{\frac{N_P}{C_P} R_{\text{CN}}, \frac{\text{Fe}_P}{C_P} R_{\text{CFe}}, 1\right\}$ (15)

218   where G is equal to G_S (equation 12a) for small zooplankton and G_P (equation 13a) for large

219   zooplankton, and R_{XY} indicates the fixed ratio of element X to element Y in grazer biomass. The

220   'excess' carbon available for respiration is

221   $$C_{XS} = G'\left\{\frac{C_P}{N_P}R_{NC} - 1, \frac{C_P}{Fe_P}R_{FeC} - 1, 0\right\} \tag{16a}$$

222   and the excess nutrients remineralized to their inorganic pools are

223   $$N_{XS} = G'\max\left\{\frac{N_P}{C_P} - R_{NC}. 0\right\}\varepsilon + G'\max\left\{R_{NC}\left(\frac{N_P}{Fe_P}R_{FeN} - 1\right). 0\right\}(1 - \varepsilon) \tag{16b}$$

224   $$Fe_{XS} = G'\max\left\{\frac{Fe_P}{C_P} - R_{FeC}. 0\right\}\varepsilon + G'\max\left\{R_{FeC}(\frac{Fe_P}{N_P}R_{NFe} - 1). 0\right\}(1 - \varepsilon) \tag{16c}$$

225   where

226   $$\varepsilon = \frac{\max\{C_{xs}, 0\}}{C_{xs} + \Delta}$$

227   is a switch to prevent double-counting in cases where one of the terms is redundant (the excess

228   relative to the least abundant element is included in the other term), but would otherwise be

229   nonzero (Δ is a constant equal to 10^{-15}, to prevent divide-by-zero). For three elements, there are

230   3! = 6 possible cases: for N greater or less than $C_P R_{NC}$, Fe may be either in excess relative to

231   both C and N, deficient relative to both, or in excess relative to one but not the other (Table 2).

232

233   Table 2 - Cases where the 'excess' terms are nonzero. These terms are always greater than or
234   equal to zero, and always zero when the phytoplankton elemental ratio is equal to the grazer bio-
235   mass ratio. A plus (+) sign indicates that a specific term is positive. N_1 and N_2, Fe_1 and Fe_2 indi-
236   cate the first and second terms in equations 16b and 16c. R_{NC} is the grazer N/C (Redfield) ratio.
237

	Fe in excess relative to both C and N					Fe in excess relative to C or N but not both					Fe deficient relative to both C and N				
	C	N_1	N_2	Fe_1	Fe_2	C	N_1	N_2	Fe_1	Fe_2	C	N_1	N_2	Fe_1	Fe_2
N/C>R_{NC}		+		+			+		+		+		+		
N/C<R_{NC}	+				+	+				+	+		+		

2.3 Organic and Inorganic Pools

238

239

240 There are two pools of detritus with different sinking rates but the same fixed elemental ratios.

241 Detrital C/N/Fe ratios are the same as zooplankton, so zooplankton mortality or grazing of small

242 zooplankton by large zooplankton produce no 'excess'. Phytoplankton mortality, and defecation

243 by zooplankton grazing on phytoplankton, produces excess nutrient or excess C that needs to be

244 recycled into the inorganic pool in a similar fashion as outlined above for the assimilated fraction

245 of grazing on phytoplankton.

246 The conservation equations for detrital C are

247
$$\frac{dD_s}{dt} = m_1(C_{ps} + Z_s) + m_2(C_{ps}^2 + Z_S^2) - r_1 D_s T_g - w_s \frac{dD_s}{dz} \tag{17a}$$

248
$$\frac{dD_l}{dt} = m_1(C_{pl} + Z_L) + m_2(C_{pl}^2 + Z_L^2) - r_2 D_l T_g - w_l \frac{dD_l}{dz} \tag{17b}$$

249 where T_g is an Arrhenius function for temperature dependence of remineralization and w is the

250 sinking speed. The conservation equations for inorganic C, N, and Fe are

251
$$\frac{dC_i}{dt} = (\zeta V^N - P_{phot}^C)C_p + R + C_{XS} + (r_1 D_s + r_2 D_l)T_g \tag{18a}$$

252
$$\frac{dN_i}{dt} = -\frac{V^N}{Q^N}N_p(\frac{L_{NO3}}{L_{NO3}+L_{NH4}}) + N_{ox} - N_{dentr}(1 - A_f) \tag{18b}$$

253
$$\frac{dN_a}{dt} = -\frac{V^N}{Q^N}N_p(\frac{L_{NH4}}{L_{NO3}+L_{NH4}}) + \frac{R}{R_{CN}} + N_{XS} + (r_1 D_s + r_2 D_l)R_{NC}T_g - N_{ox} + N_{dnf} - N_{dentr}A_f \tag{18c}$$

254
$$\frac{dFe}{dt} = \frac{V^{Fe}}{Q^{Fe}}Fe_p + \frac{R}{R_{CFe}} + Fe_{XS} + (r_1 D_s + r_2 D_l)R_{FeC}T_g \tag{18d}$$

255 where N_{ox} is microbial oxidation of ammonium to nitrate (nitrification), N_{dnf} and N_{dentr} are

256 sources and sinks associated with dinitrogen fixation and denitrification, and A_f is the ammonium

257 fraction of denitrification losses, associated with anaerobic ammonium oxidation ("anammox").

15

258   The oxygen equation is essentially the inverse of equation 18a, with additional terms for

259   oxidation and reduction of N, i.e.,

260    $\frac{dO_2}{dt} = -\frac{dC_i}{dt} + 2\frac{V^N}{Q^N}N_p\left(\frac{L_{NO3}}{L_{NO3}+L_{NH4}}\right) - 2N_{ox}$ (19)

261   Nitrification is given by

262    $N_{ox} = k_{NH4ox}N_a\frac{K_E}{K_E+E(z)}$ (20)

263   where $E(z)$ is the layer mean irradiance at depth z. Dinitrogen fixation is parameterized as an

264   external input of ammonium dependent on light, temperature and Fe availability, and inhibited

265   by high ambient concentrations of inorganic N,

266    $N_{dnf} = k_{dnf}T_{dnf}(1 - e^{-aE})\left(\frac{Fe}{K_{Fe}+Fe}\right)\left(\frac{K_{NO3}}{K_{NO3}+N_i+N_a}\right)$ (21)

267   where $T_{dnf}=\max(0, 1.962(T_f - 0.773))$, i.e., a linear multiple of equation (1) that is 0 at T<20°C

268   and unity at T=30°C.

269

270   Denitrification is parameterized as a fraction of total remineralization that increases as a linear

271   function of oxygen concentration for concentrations less than a threshold concentration O_{mxd}

272    $N_{frxn} = 1 - \frac{\min(O_2,O_{mxd})}{O_{mxd}}$ (22)

273   Remineralization is then divided among oxygen (1-N_{frxn}), nitrate (0.875N_{frxn}), and ammonium

274   (0.125N_{frxn}) assuming an average anammox contribution of 25% (Babbin et al., 2014). We use

275   this average ratio of anammox to classical denitrification to partition fixed N losses between

276   NO_3^- and NH_4^+; the DIC sink and organic matter source associated with anammox are small and

277   are neglected here.

278

2.4 Calcification, Calcite Dissolution, and Alkalinity

Calcification is represented by a detrital calcium carbonate (CaCO$_3$) state variable, but no explicit calcifier groups. Detrital CaCO$_3$ sinks in the same fashion as detrital particulate organic carbon (POC), with a sinking rate independent of those for large and small organic detritus. Calcite production is represented as a fixed fraction of detritus production from small phytoplankton and small zooplankton mortality:

$$\frac{dCa}{dt} = m_1\left(C_{\text{ps}} + Z_s\right)P_{Ca} + m_2\left(C_{ps}^2 + Z_S^2\right)P_{Ca} - k_{Ca}Ca - w_{Ca}\frac{dCa}{dz} \tag{23}$$

Calcite dissolution occurs throughout the water column as a first order process (i.e., no dependence on temperature or saturation state). Approximately 80% of calcite produced is exported from the euphotic zone. Burial in the sediments is represented as a simple 'on/off' switch dependent on the calcite saturation state (zero when Ω_C<1 and 1 when Ω_C≥1). Calcite burial is balanced by an equivalent source of DIC and alkalinity at the ocean surface as a crude parameterization of fluvial sources.

For each mole of calcite production two moles of alkalinity equivalent are lost from the dissolved phase; the reverse occurs during calcite dissolution. There are additional sources and sinks for alkalinity associated with phytoplankton nutrient uptake, organic matter remineralization, nitrification, denitrification and dinitrogen fixation (Wolf-Gladrow et al., 2007, see Supplementary Table S2). The anammox reaction does not in itself contribute to alkalinity (Jetten at al., 2001), but there is a sink associated with ammonium oxidation to nitrite (the model does not distinguish between nitrite and nitrate). Autotrophic production of organic matter by anammox bacteria is a net source of alkalinity (Strous et al., 1998) but this source is extremely

302 small (~0.03 mol/molN) and is neglected here. Globally, the sources and sinks of alkalinity from

303 the N cycle offset each other such that there is no net gain or loss as long as the global fixed N

304 pool is conserved (see below Sect. 2.5). If dinitrogen fixation and denitrification are allowed to

305 vary freely, there will generally be a net gain or loss of fixed N and, therefore, of alkalinity.

306

307 **2.5 External Nutrient Sources and Sinks**

308

309 External sources and sinks consist of river inputs, aeolian deposition, biological N_2 fixation, de-

310 nitrification, mobilization of Fe from reducing sediments, loss of Fe to scavenging, and burial of

311 calcium carbonate in the sediments. Aeolian deposition of Fe is calculated from a climatology of

312 mineral dust deposition generated from offline (atmosphere-only) simulations with CanAM4

313 (von Salzen et al., 2013), with an Fe mass fraction of 5% and a fractional solubility of 1.4% in

314 the surface layer. Subsurface dissolution is parameterized based on PISCES (Aumont et al.,

315 2015); the total dissolution is 6.35%, with 22% of soluble Fe input into the first vertical layer

316 (see Supplementary material). Iron from reducing sediments is also based on PISCES, with a

317 constant areal flux of 1000 nmol m^{-2} d^{-1} in the first model level, declining exponentially with in-

318 creasing seafloor depth (i.e., assuming that the sediments become progressively more oxygen-

319 ated) with an e-folding length scale of about 200 m. Scavenging of dissolved iron is first-order

320 with a high rate (2.5 d^{-1}) for concentrations in excess of 0.6 nM (Johnson et al., 1997). For con-

321 centrations below this threshold, the rate is much lower (0.001 d^{-1}) and is weighted by the con-

322 centration of organic detritus (Christian et al., 2002b), i.e.,

323 $\frac{dFe}{dt} = -FeS_{Fe1}min\{(D_S + D_L)P_{Fe}, 1\}$ (24)

324   where Fe is the dissolved iron concentration, D_S and D_L are the small and large detritus concen-

325   trations, S_{Fe1} is the first-order scavenging rate in surface waters with abundant particulates, and

326   P_{Fe} is an empirical parameter to determine the dependence on particle concentration (Table 1).

327   The basis for this parameterization is that the rate of scavenging must depend not only on the

328   concentration of iron but on the concentration of particles available for it to precipitate onto, and

329   assumes that POC is strongly positively correlated with total particulate matter. Scavenging is

330   treated as irreversible, i.e., scavenged Fe is not tracked and does not reenter the dissolved phase.

331

332   Unlike in CMOC, N_2 fixation and denitrification vary independently in CanOE, so the global

333   total N pool can change. Conservation is imposed by adjusting the global total N pool according

334   to the difference between the gain from N_2 fixation and the loss to denitrification. A slight

335   adjustment is applied to the nitrate concentration at every grid point, while preserving the overall

336   spatial structure of the nitrate field. Adjustments are multiplicative rather than additive to avoid

337   producing negative concentrations. This adjustment does not maintain (to machine precision) a

338   constant global N inventory but is intended to minimize long term drift, keeping it much smaller

339   than the free surface error (see below). This adjustment is applied every 10 days and has a

340   magnitude of approximately 7×10^{-8} of the total N.

341

342   One mole of alkalinity is removed per mole of N added or removed, since there are alkalinity

343   sources of 1 mol/molN associated with both N_2 fixation (creation of new NH_4^+) and

344   denitrification (removal of NO_3^-), offset by a 2 mol/molN sink associated with nitrification. As

345   noted above, $CaCO_3$ can dissolve or be buried in the sediments depending on the calcite

346   saturation. DIC and alkalinity lost to burial are reintroduced at the ocean surface, at the same grid

347   point as burial occurs, providing a crude parameterization of river inputs so that global

348   conservation is maintained (fresh water runoff contains no DIC or alkalinity). However, the OPA

349   free surface formulation is inherently imperfect with regard to tracer conservation. Drift in total

350   ocean alkalinity and nitrogen over time is on the order of 0.01% and 0.03% per thousand years,

351   respectively (losses due to the free surface are generally larger for tracers with less homogeneous

352   distributions).

353

354   **2.6 Ancillary data**

355

356   For first-order model validation we have relied largely on global gridded data products rather

357   than individual profile data. Global gridded data from World Ocean Atlas 2013 (WOA2013)

358   (Locarnini et al., 2013; Zweng et al., 2013; Garcia et al., 2014a; 2014b) were used for

359   temperature, salinity, and oxygen and nitrate concentration. DIC and alkalinity were taken from

360   the GLODAP gridded data product (Lauvset et al., 2016). Offline carbon chemistry calculations

361   were done following the Best Practices Guide (Dickson et al., 2007) and the OMIP-BGC

362   protocols (Orr et al., 2017), which are identical to those used in the models except that constant

363   reference concentrations were used for phosphate (1 µM) and silicate (10 µM).

364

365   There is no global gridded data product for Fe, but we have made use of the GEOTRACES

366   Intermediate Data Product 2017 (Schlitzer et al., 2018), and the data compilations from MBARI

367   (Johnson et al., 1997; 2003) and PICES Working Group 22 (Takeda et al., 2013). The latter two

368   are concentrated in the Pacific, while GEOTRACES is more global. The combined data sets

369   provide more than 10000 bottle samples from more than 1000 different locations (Supplementary

370   Figure S4a) (excluding some surface transect data that involve frequent sampling of closely

371   spaced locations along the ship track). More detail about model comparison to these data

372   compilations and the list of original references are given in the Supplementary information.

373

374   Satellite ocean colour estimates of surface chlorophyll were taken from the combined

375   SeaWiFS/MODIS climatology described by Tesdal et al. (2016). Climatological satellite POC

376   was downloaded from the NASA ocean colour web site and is based on the algorithm of

377   Stramski et al. (2008) using MODIS-Aqua data. This climatology differs slightly from the

378   chlorophyll one in terms of years included and sensors utilized, but as only climatological

379   concentrations are considered and each climatology covers ~15 years, these differences will have

380   negligible effect on the results presented.

381

382   CMIP6 model data were regridded to a common grid (2x2°, 33 levels following the GLODAP

383   levels) to facilitate ensemble averaging. The years 1986-2005 of the Historical experiment were

384   averaged into climatologies or annual means, for meaningful comparison with observation-based

385   data products. A single realization was used in each case; as 20 year averages are used, internal

386   variability is assumed to have little effect (e.g., Arguez and Vose, 2011). Sampling among

387   CMIP6 models was somewhat opportunistic and the exact suite of models varies among the

388   analyses presented. When we conducted a search for a particular data field, we included in the

389   search parameters all models that published that field, and repeated the search at least once for

390   models that were unavailable the first time the search was executed. In some cases, model

391   ensemble means excluded all but one model from a particular 'family' (e.g., there are three

392   different MPI-ESM models for which ocean biogeochemistry fields were published), as the

393   solutions were found to be similar and would bias the ensemble mean towards their particular

394   climate. More detail is given in Supplementary Table S3.

395

396   **3. Results**

397

398   **3.1 Distribution of oxygen**

399

400   The spatial distribution of oxygen concentration ($[O_2]$) at selected intermediate depths (400, 900,

401   and 1400 m) for CanESM5, CanESM5-CanOE, a model ensemble mean (MEM) of CMIP6

402   models (excluding CanESM5 and CanESM5-CanOE), and gridded data from WOA2013 is

403   shown in Figure 2. The major features are consistent across the models. All three cases show

404   elevated oxygen concentrations relative to observations, particularly in the North Pacific, the

405   North Atlantic and the Southern Ocean. In the Indian Ocean, both CanESM models show high

406   oxygen concentrations in the Arabian Sea and deeper layers of the Bay of Bengal relative to

407   observations and other CMIP6 models; these biases are somewhat smaller in CanESM5-CanOE

408   than in CanESM5 (Figure 2).

409

410   Biases in the eastern boundary current regions are depth and model specific. CanESM5 shows

411   particularly strong oxygen depletion at 1400 m in the eastern tropical Pacific. In the southeastern

412   Atlantic, models tend to be biased low at the shallower depths, and show somewhat more

413   variation at greater depths (Figure 2). Overall, $[O_2]$ biases tend to be positive over large areas of

414   ocean with the exception of some eastern boundary current regions, implying that models

415   exaggerate the extent to which remineralization is concentrated in these regions. An alternate
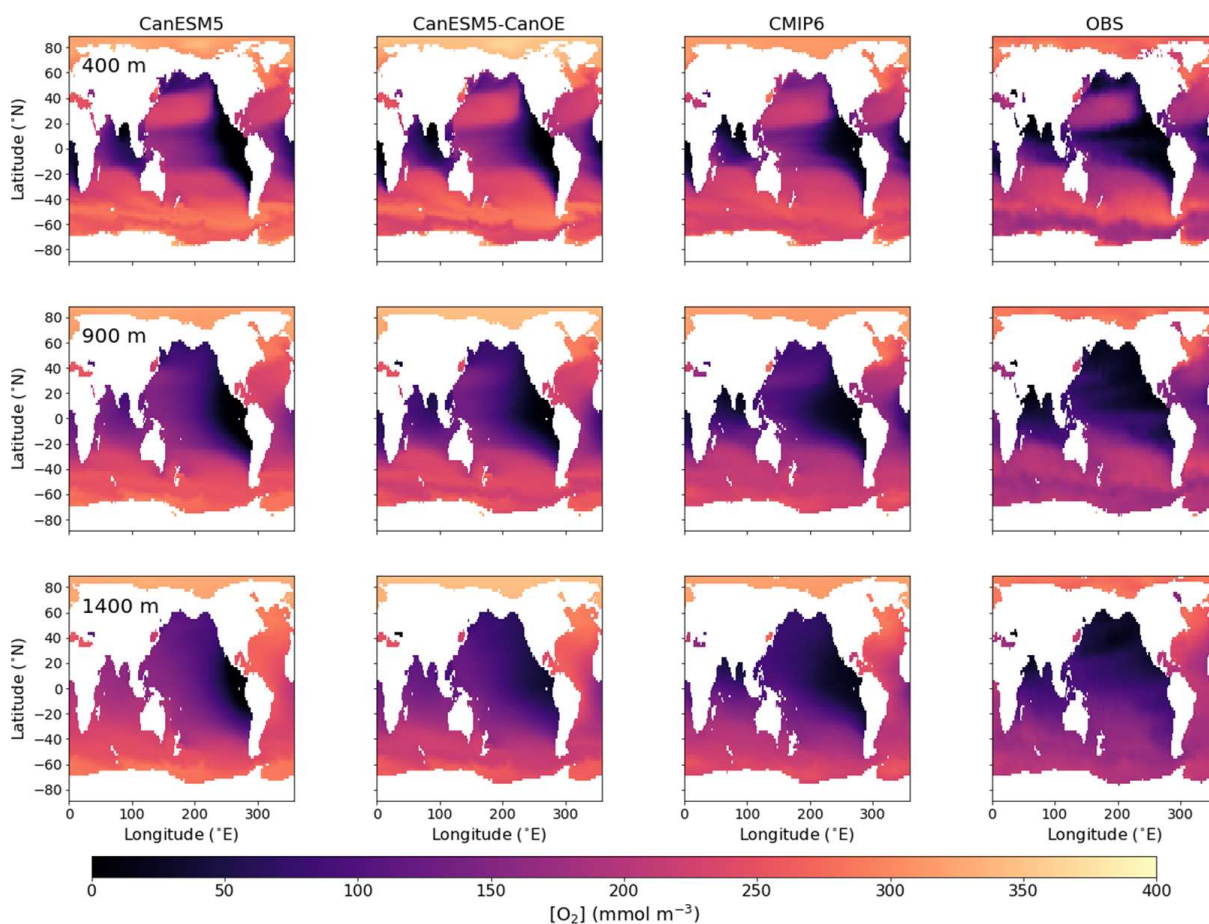
Figure 2 - Global distribution of oxygen (O_2) concentration in mmol m^{-3} at 400, 900, and 1400 m (rows) for CanESM5-CanOE, CanESM5, the mean for other (non-CanESM) CMIP6 models, and World Ocean Atlas 2013 (WOA2013) observations (columns). Difference from the observation-based fields are shown in Supplementary Figure S3.

417   version of Figure 2 that shows model errors relative to the observational data product is given in

418   Supplementary Figure S3.

419

420   The zonal mean oxygen concentration, saturation concentration, and apparent oxygen utilization

421   (AOU) are shown in Figure 3 for the same four cases. Again, the models generally show a

422   positive bias in [O_2], particularly in high-latitude deep waters. The major ocean circulation

423   features are reproduced fairly well in all cases (e.g., weaker ventilation of low-latitude

424   subsurface waters, greater vertical extent of well-ventilated surface waters in the subtropics). The

425   saturation concentration (a function of temperature and salinity) generally shows relatively little

426   bias, implying that the bias in [O_2] arises mainly from remineralization and/or ventilation. AOU

427   is lower than observed over much of the subsurface ocean. Regional biases are quite consistent

428   across models, but are slightly greater in CanESM5 than in CanESM5-CanOE or the ensemble

429   mean, except in the Arctic Ocean. Again, Supplementary Figure S3 includes a version of this

430   plot that shows the model differences from the observations.

431

432   The skill of each model with respect to the distribution of O_2 at different depths is represented by

433   Taylor diagrams (Taylor, 2001) in Figure 4, in which all of the CMIP6 models that were shown

434   as an ensemble mean in Figures 2 and 3 are shown individually. The blue dots represent

435   CanESM5, red CanESM5-CanOE, and grey the ensemble mean of all CMIP6 models except

436   CanESM5 and CanESM5-CanOE; the smaller grey dots represent the individual models.

437   CanESM5-CanOE shows slightly higher pattern correlation than CanESM5 at all depths. Both

438   models compare favourably with the full suite of CMIP6 models, with r>0.85 for CanESM5 and

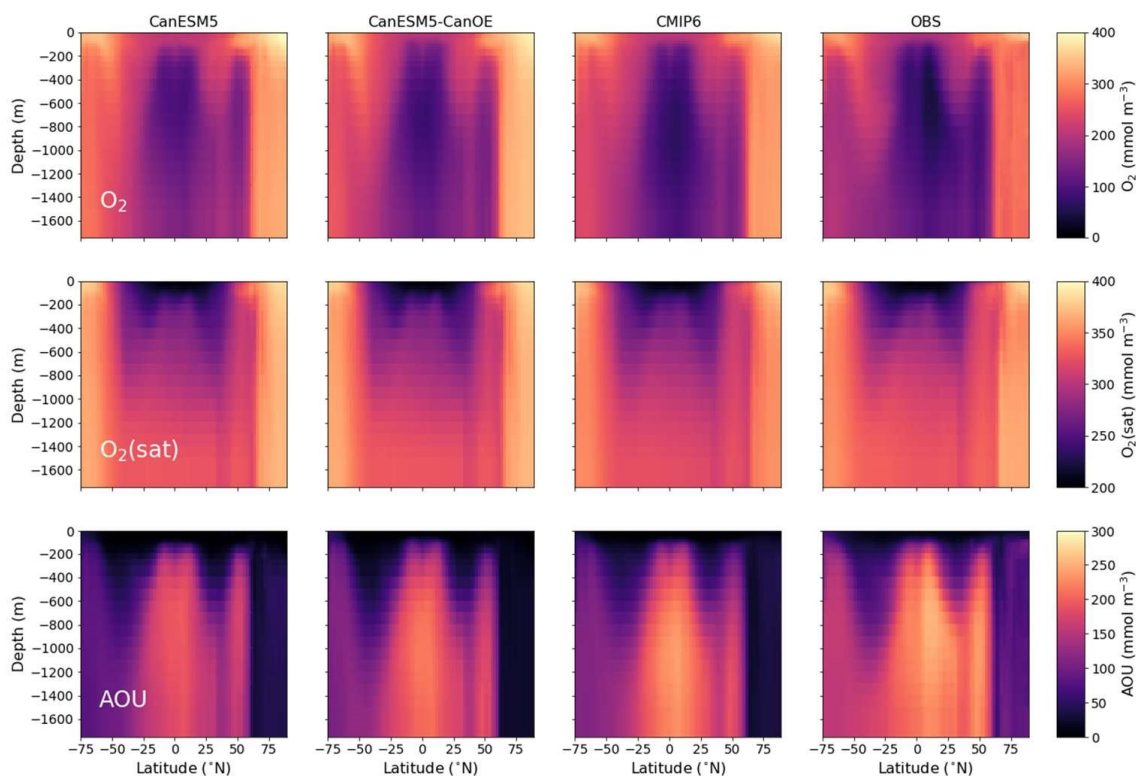439   r>0.9 for CanESM5-CanOE at all depths examined, and a normalized standard deviation within

Figure 3 - Latitude-depth distribution (surface to 1750 m) of zonal mean oxygen concentration (O_2), oxygen concentration at saturation (O_2(sat)), and apparent oxygen utilization (AOU) in mmol m^{-3} for CanESM5-CanOE, CanESM5, the mean for other CMIP6 models, and observations (WOA2013). Note different colour scales for different rows. Difference from the observation-based fields are shown in Supplementary Figure S3.
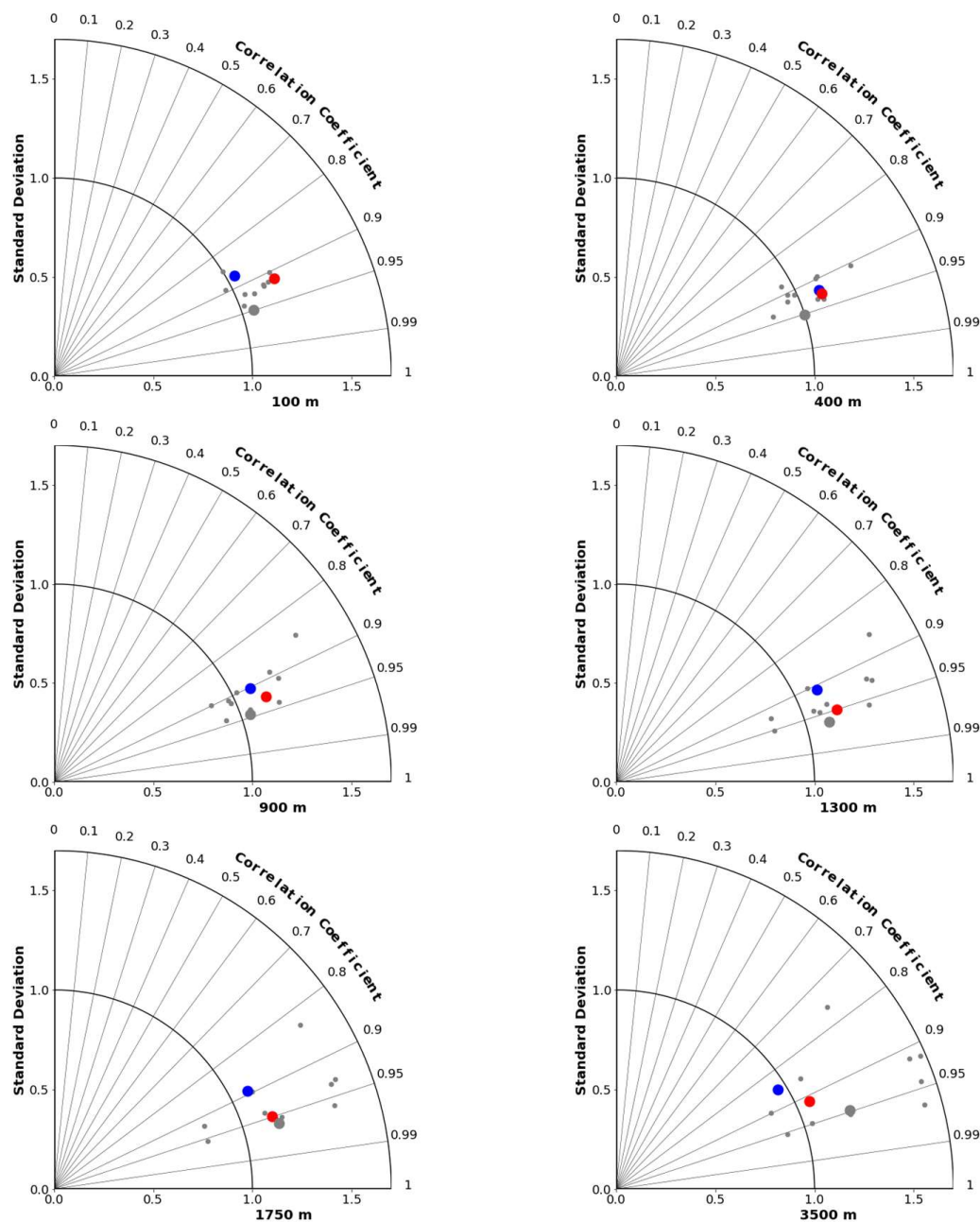
Figure 4 - Taylor diagrams (Taylor, 2001) comparing modelled and observed distributions of oxygen at specific depths from 100 to 3500 m. Angle from the vertical indicates spatial pattern correlation. Distance from the origin indicates ratio of standard deviation in modelled vs. observed (WOA2013) fields. Red dots represent CanESM5-CanOE, blue dots CanESM5, small grey dots other CMIP6 models, and large grey dots the model ensemble mean for all CMIP6 models except CanESM5 and CanESM5-CanOE.

26

442   ±25% of unity.

443

444   The total volume of ocean with [O_2] less than 6 mmol m^{-3} (the threshold for denitrification

445   (Devol, 2008)) and 60 mmol m^{-3} (a commonly used index of hypoxia) is shown in Figure 5. The

446   total volume is highly variable among models (note, however, that there are several clusters of

447   related models with quite similar totals). CanESM5 and CanESM5-CanOE have among the

448   lowest total volumes (i.e., the interior ocean is relatively well ventilated) and are among the

449   nearest to the observed total. For [O_2] <60 mmol m^{-3} the bias is, nonetheless, quite large (i.e., the

450   observed volume is underestimated by almost 50% in both models). The volume of water with

451   [O_2] below the denitrification threshold is overestimated in both CanESM5 and CanESM5-

452   CanOE; CanESM5-CanOE has a much smaller total that is closer to the observed value. The bias

453   in the spatial pattern of hypoxia (not shown) is generally similar to the bias in dissolved oxygen

454   distribution (Figure 2). The low-oxygen regions are generally more concentrated in the eastern

455   tropical Pacific in the models than in observations, and the low-oxygen region in the northwest

456   Pacific is not well reproduced in CanESM models.

457

458   **3.2 Distribution of DIC, alkalinity, and CaCO$_3$ saturation**

459

460   The spatial distribution of aragonite saturation state (Ω_A) at selected depths is shown in Figure 6

461   (the first two depths are the same as in Figure 2, but the third is much deeper). In this case the

462   observations are a combination of GLODAP (Lauvset et al., 2016) for DIC and alkalinity, and

463   WOA2013 for temperature and salinity. CanESM5 and CanESM5-CanOE generally compare

464   well with other models and observations. The low saturation bias in the eastern tropical Pacific is
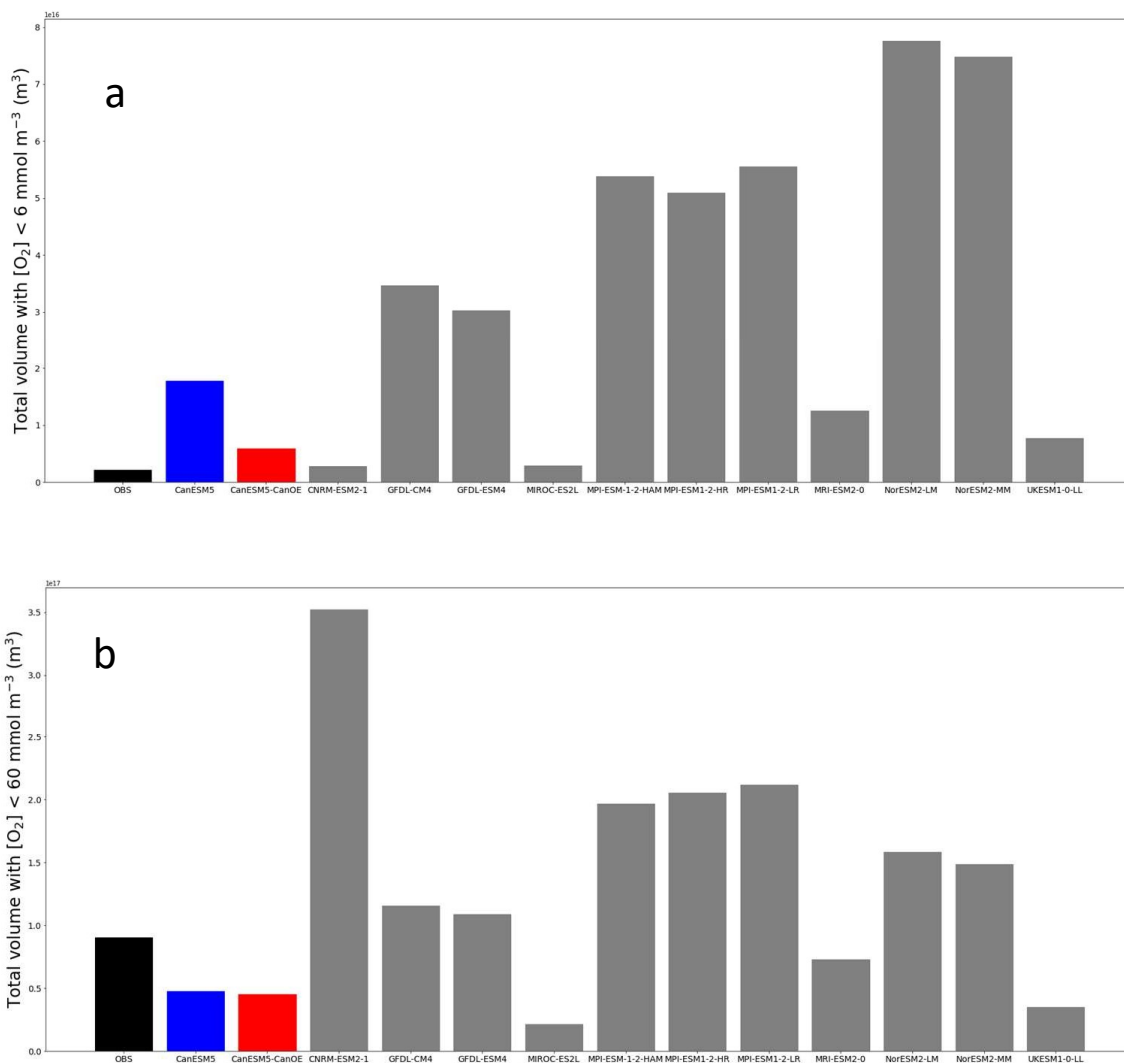
Figure 5 - Total volume of ocean with oxygen (O_2) concentration less than (a) 6 mmol m^{-3} (mean for last 30 years of the historical experiment) and (b) 60 mmol m^{-3}. Observation are from WOA2013.
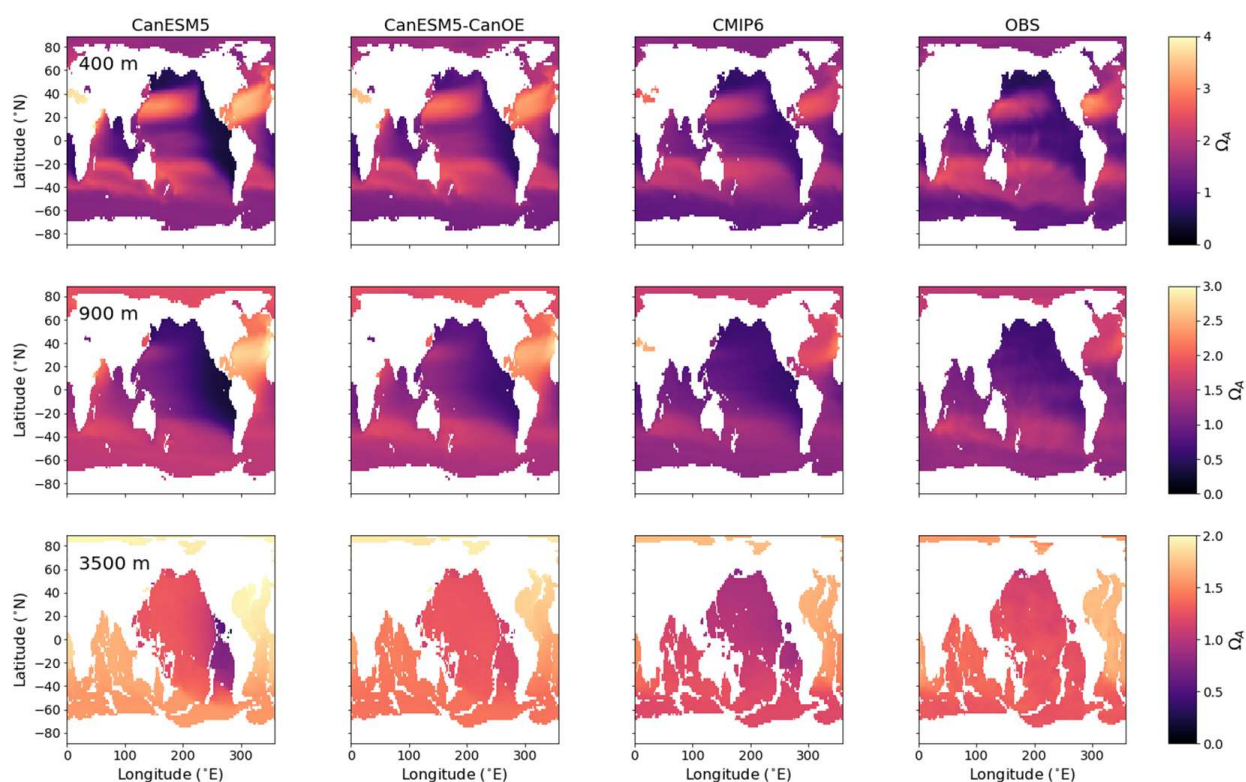
Figure 6 - Global distribution of aragonite saturation (Ω_A) at 400, 900, and 3500 m for CanESM5-CanOE, CanESM5, the mean for other CMIP6 models, and observations (GLODAP + WOA2013). Note different colour scales for different depths. Difference from the observation-based fields are shown in Supplementary Figure S3.

467   substantially reduced in CanESM5-CanOE compared to CanESM5. On the other hand CanESM5

468   generally does better than CanESM5-CanOE, or the ensemble mean, at reproducing the low

469   saturation states in the northwestern Pacific and the Bering Sea. Both models show a high

470   saturation state bias in the North Atlantic and the well-ventilated regions of the north Pacific

471   subtropical gyre. These biases are reduced slightly in CanESM5-CanOE, probably due to the

472   smaller average remineralization length scale for organic detritus.

473

474   Zonal mean distributions of aragonite saturation state (Ω_A), calcite saturation state (Ω_C), and

475   carbonate ion concentration ($[CO_3^{--}]$) are shown in Figure 7 (Supplementary Figure S3 includes

476   versions of Figures 6 and 7 that explicitly show the model differences from the observations).

477   The models generally compare well with the observations in the representation of the

478   latitude/depth distribution of high and low saturation waters. CanESM5 has a high saturation bias

479   in low-latitude surface waters that is somewhat reduced in CanESM5-CanOE. Both CanESM5

480   models show a high saturation bias in Northern Hemisphere intermediate (e.g., 200-1000 m)

481   depth waters that is larger than in the ensemble mean.

482

483   Taylor diagrams for a range of depths are shown for DIC in Figure 8 and for Ω_A in Figure 9 (for

484   alkalinity, see Supplementary Figure S2). As expected, the MEM generally compares favourably

485   with the individual models (e.g., Lambert and Boer, 2001). CanESM5 and CanESM5-CanOE

486   compare favourably with the full suite of CMIP6 models. CanESM5-CanOE shows a gain in

487   skill relative to CanESM5, and both show improvement relative to CanESM2. At 400 m,

488   CanESM2 stands out as having extremely high variance, which is mostly due to extremely high

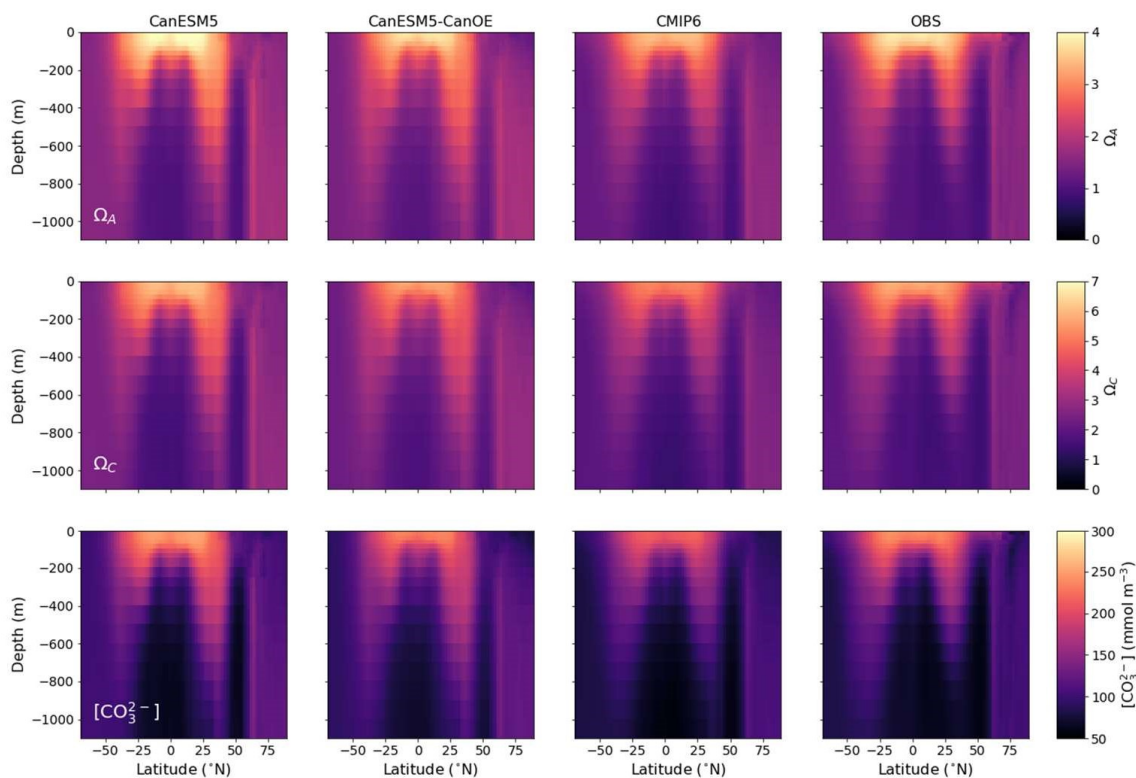489   DIC concentrations occurring over a limited area in the eastern equatorial Pacific (not shown).

Figure 7 - Latitude-depth distribution of zonal mean (surface to 1150 m) aragonite saturation state (Ω_A), calcite saturation state (Ω_C), and carbonate ion concentration ([CO3--]) in mmol m^{-3} for CanESM5-CanOE, CanESM5, the mean for other CMIP6 models, and observations (GLODAP + WOA2013). Difference from the observation-based fields are shown in Supplementary Figure S3.
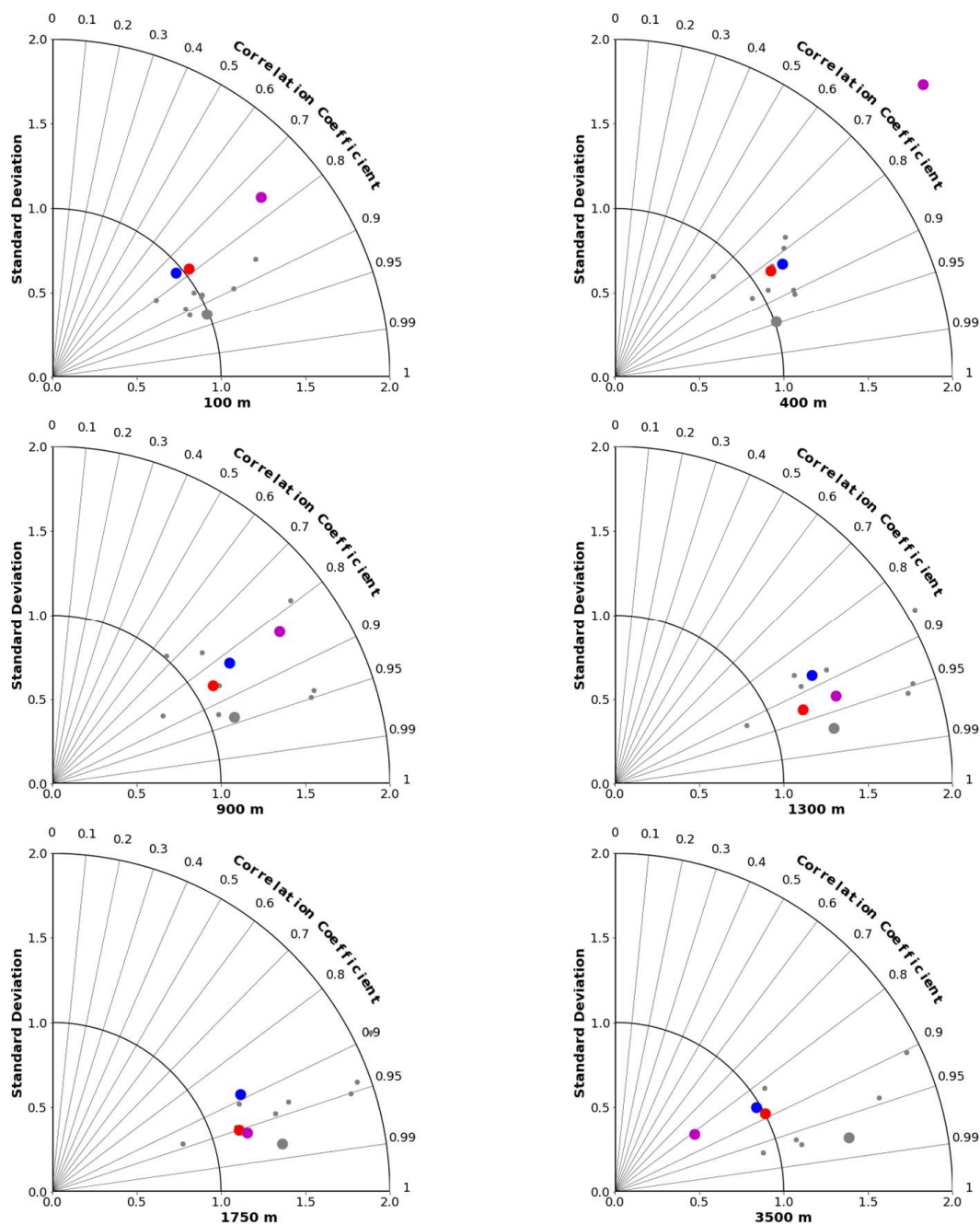
Figure 8 - Taylor diagrams comparing modelled and observed distributions of DIC at specific depths from 100 to 3500 m. Observations are from GLODAP (Lauvset et al., 2016). Red dots represent CanESM5-CanOE, blue dots CanESM5, magenta dots CanESM2, small grey dots other CMIP6 models, and large grey dots the model ensemble mean for all CMIP6 models except CanESM5 and CanESM5-CanOE.
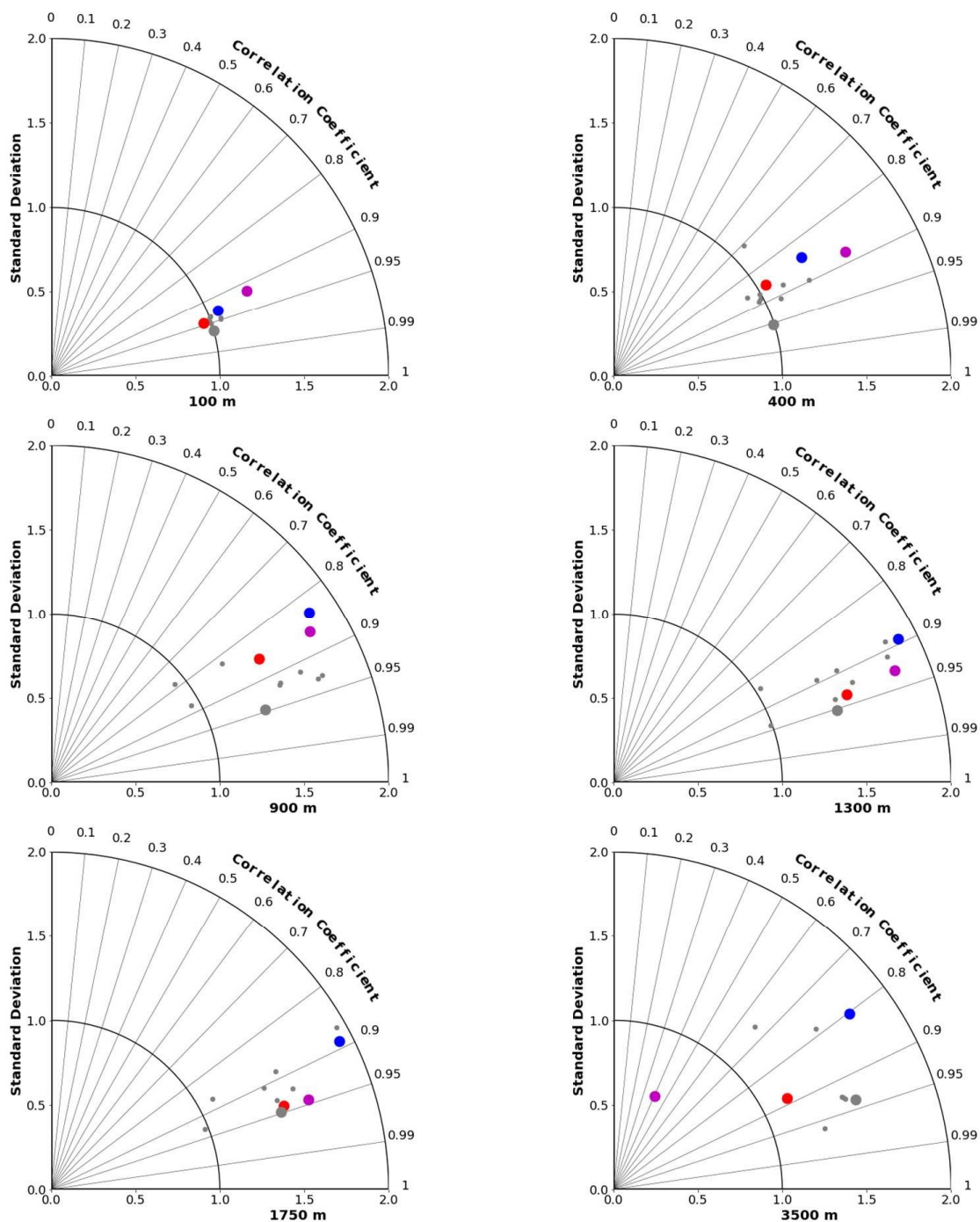
Figure 9 - Taylor diagrams comparing modelled and observed (GLODAP + WOA2013) distributions of Ω_A at specific depths from 100 to 3500 m. Symbol colours as in Figure 8.

493 This bias is present in CanESM5 and in CMIP6 models generally (Figure 6) but involves much

494 lower concentrations spread over a larger area.

495

496 **3.3 N and Fe cycles**

497

498 An important difference between CMOC and CanOE is the inclusion of a prognostic Fe cycle.

499 The CMOC iron mask (Zahariev et al., 2008) was a pragmatic solution in the face of resource

500 limitations but is inherently compromised as it can not evolve with a changing climate. Other

501 centres that introduced a prognostic Fe cycle between CMIP5 and CMIP6 include JAMSTEC

502 (MIROC-ESM, MIROC-ES2L) and the UK Met Office (HadGEM2-ES, UKESM1-0-LL). The

503 first order test of a model with prognostic, interacting Fe and N cycles is whether it can

504 reproduce the distribution of High-Nutrient, Low-Chlorophyll (HNLC) regions and the

505 approximate surface macronutrient concentrations within these. CanESM5-CanOE succeeded by

506 this standard, although the surface nitrate concentrations are biased low in the subarctic Pacific

507 and equatorial Pacific and high in the Southern Ocean and in the global mean (Figure 10).

508

509 The seasonal cycle of the zonal mean surface nitrate concentration for a selection of CMIP6

510 models is shown in Figure 11. CanESM5, CanESM5-CanOE, and CNRM-ESM2-1 reproduce the

511 equatorial enrichment and the low concentrations in the tropical-subtropical latitudes fairly well.

512 Some models either have very weak equatorial enrichment (MPI-ESM1-2-LR) or too high a

513 concentration in the off-equatorial regions (UKESM1-0-LL, NorESM2-LM). UKESM1-0-LL

514 has very high concentrations throughout the low-latitude Pacific, which biases the ensemble

515 mean (Figure 11a). Figure 11b shows the same data as Figure 11a but for a more limited latitude
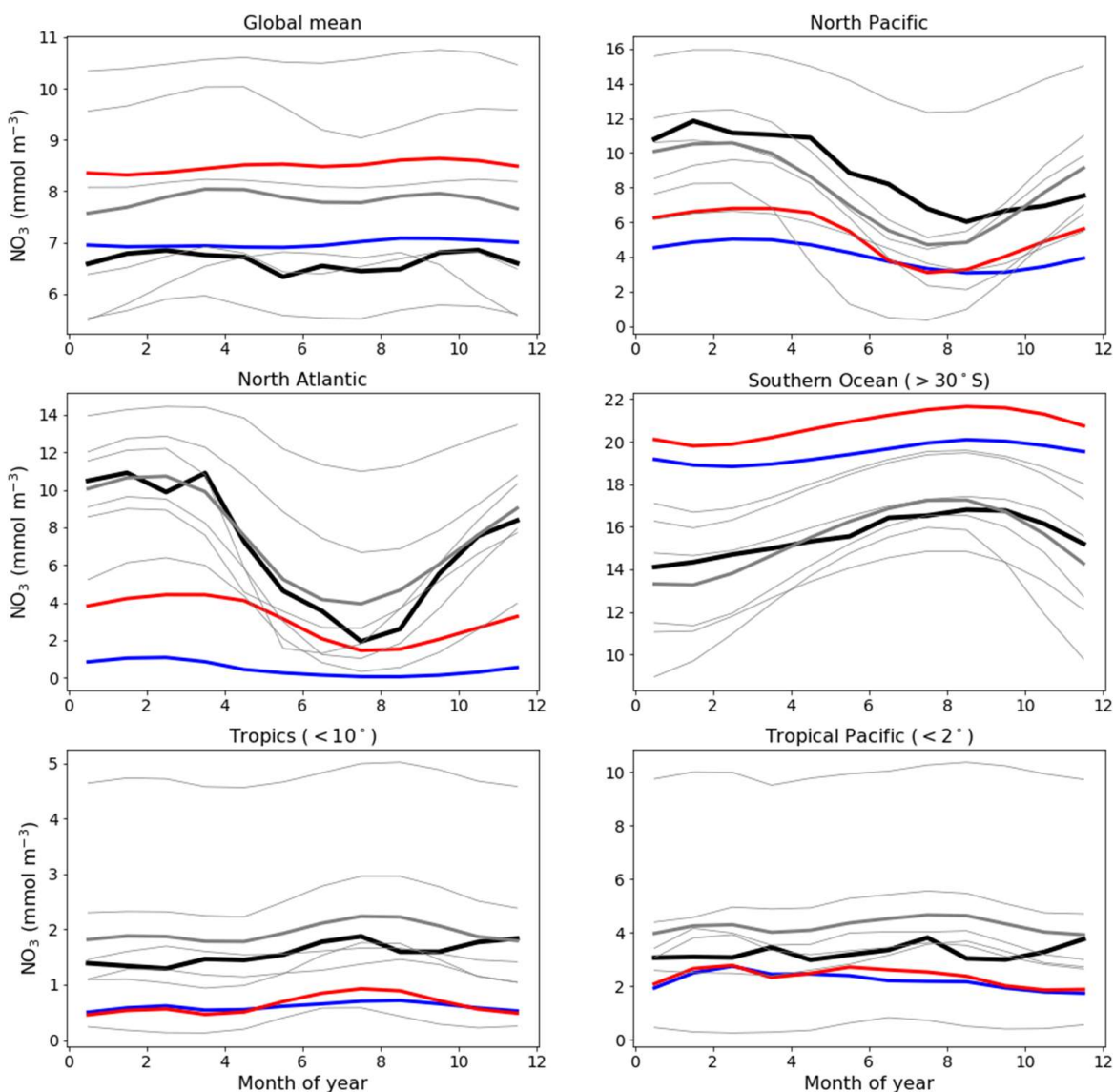
Figure 10 - Climatological seasonal cycle of surface nitrate concentration averaged for selected ocean regions. Thick red line represents CanESM5-CanOE, thick blue line CanESM5, thick black line observations (WOA2013), thin grey lines individual CMIP6 models, and thick grey line the model ensemble mean (excluding CanESM5 and CanESM5-CanOE). Regional boundaries are given in Supplementary Table S4.
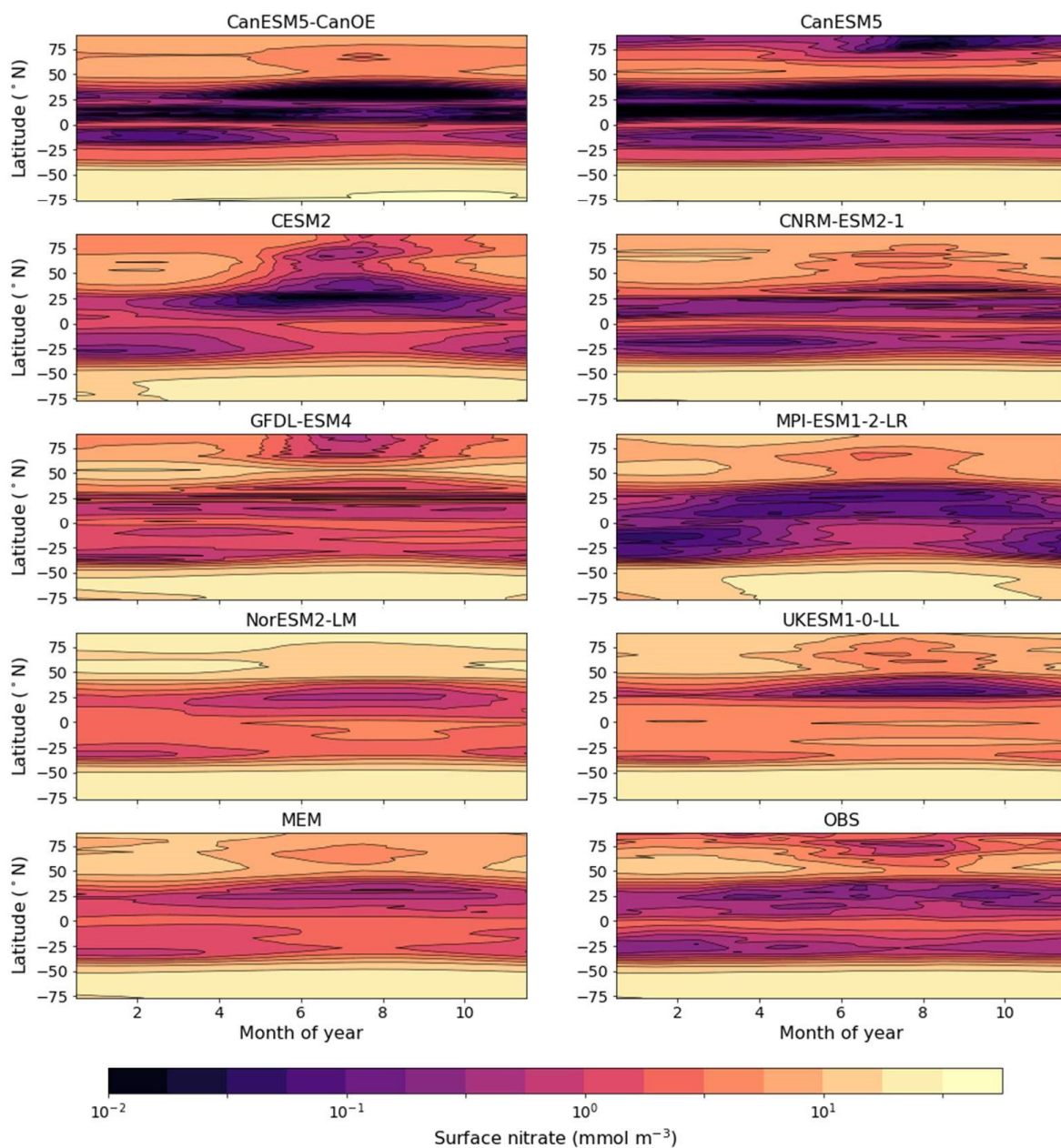
Figure 11 - (a) Climatological seasonal cycle of zonal mean surface nitrate concentration, for a selection of CMIP6 models, a model ensemble mean (MEM) excluding CanESM5 and CanESM5-CanOE, and an observation-based data product (WOA2013).
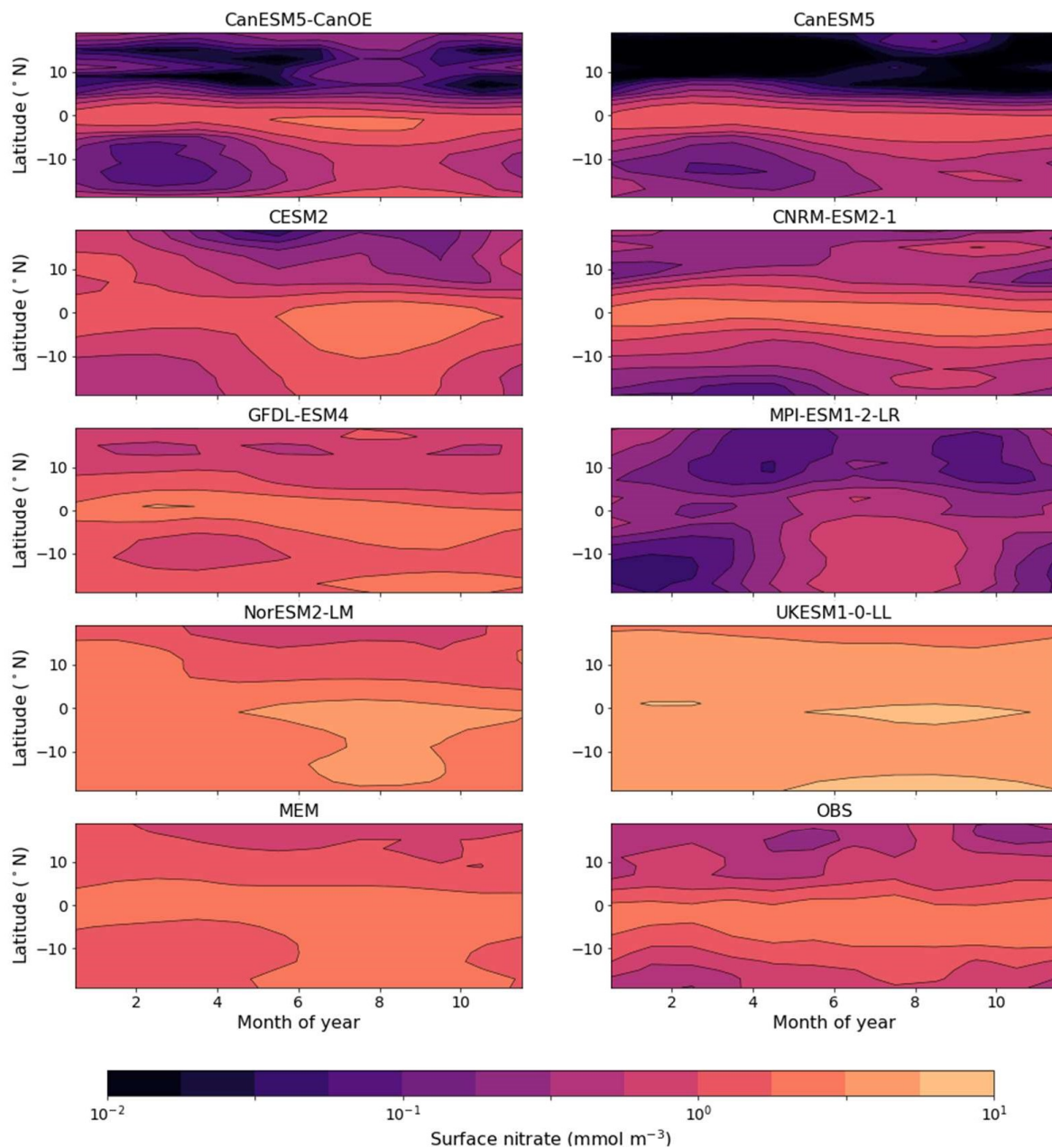
Figure 11 (b) As Figure 11(a) but for latitudes <20°.

519 range to better illustrate model behaviour in the tropics. CanESM5, CanESM5-CanOE, and

520 CNRM-ESM2-1 reproduce the seasonal cycle of tropical upwelling (e.g., Philander and Chao,

521 1991), with highest concentrations in summer.

522

523 The surface distribution of dissolved iron (dFe) in various CMIP6 models is shown in Figure 12.

524 For Fe there is no observation-based global climatology with which to compare the model

525 solutions (some comparisons to available profile data are shown in Supplementary Figures S4b-

526 g). CanESM5-CanOE shows a similar overall spatial pattern to other models, and generally falls

527 in the middle of the spread, particularly regarding concentrations in the Southern Ocean. Several

528 models show extremely high concentrations in the tropical-subtropical North Atlantic (Sahara

529 outflow region). CanESM5-CanOE, along with CNRM-ESM2-1 and CESM2, has much less

530 elevated concentrations in this region, due to lower deposition or greater scavenging or both.

531 CanESM5-CanOE has its lowest concentration in the eastern subtropical South Pacific, which is

532 common to many models (Figure 12). The area of strong surface depletion is generally more

533 spatially restricted in CanESM5-CanOE than in other models, and surface dFe concentrations are

534 greater over large areas of the Pacific. Both the north-south and east-west asymmetry of

535 distribution in the Pacific is greater in CanESM5-CanOE than in most other models, some of

536 which show the South Pacific minimum extending westward across the entire basin, and others

537 into the Northern Hemisphere. Only in CESM2 is this minimum similarly limited to the

538 southeast Pacific.

539

540 The mean depth profiles of dFe are shown in Figure 13. Some models show more of a "nutrient-

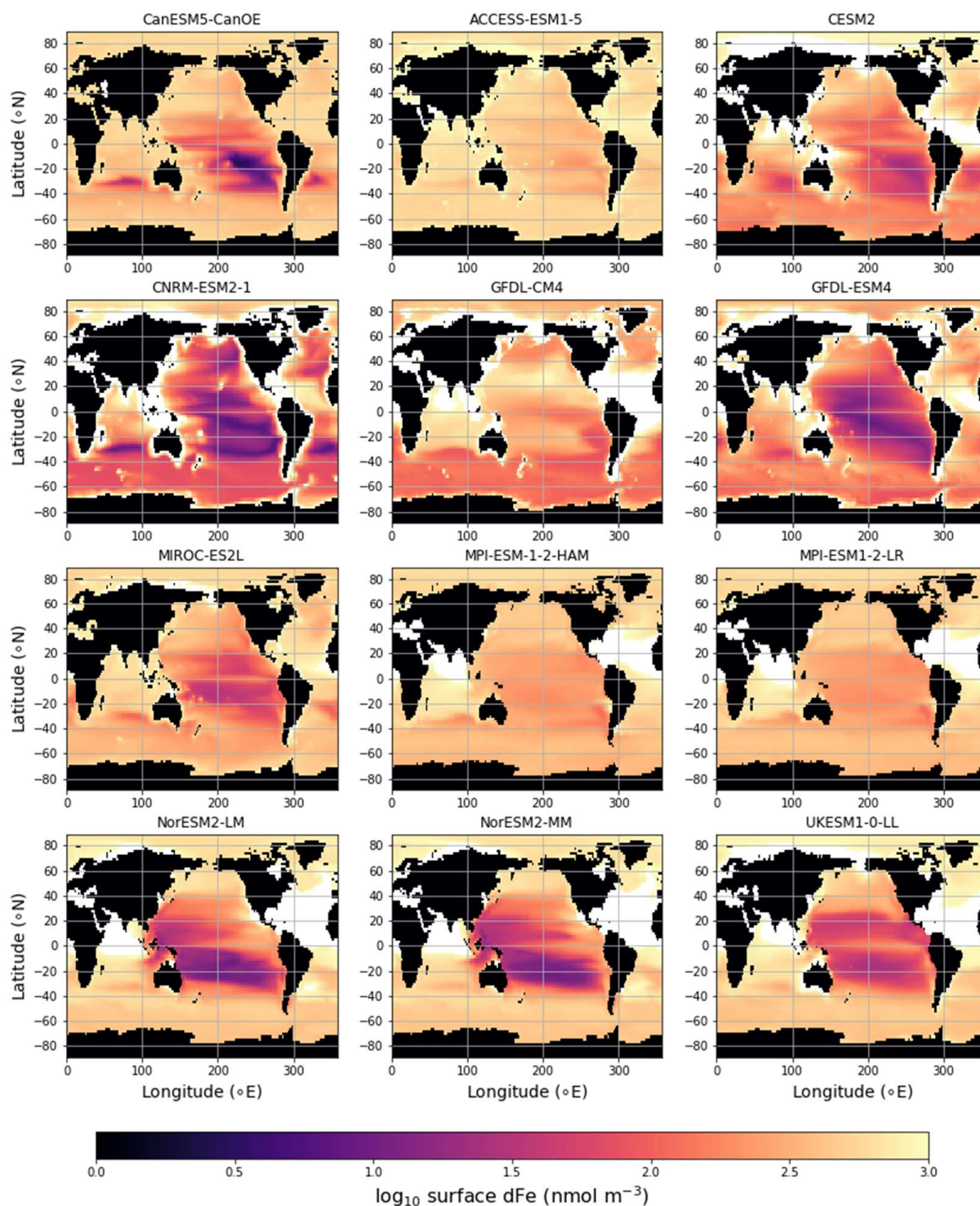541 type" (increasing with depth due to strong near-surface biological uptake and subsequent

Figure 12 - Global distribution of dissolved iron (dFe) concentration (log10 of concentration in nmol m^{-3}) at the ocean surface for CanESM5-CanOE and other CMIP6 models that published this field. Concentrations exceeding 1000 nmol m^{-3} are masked white.
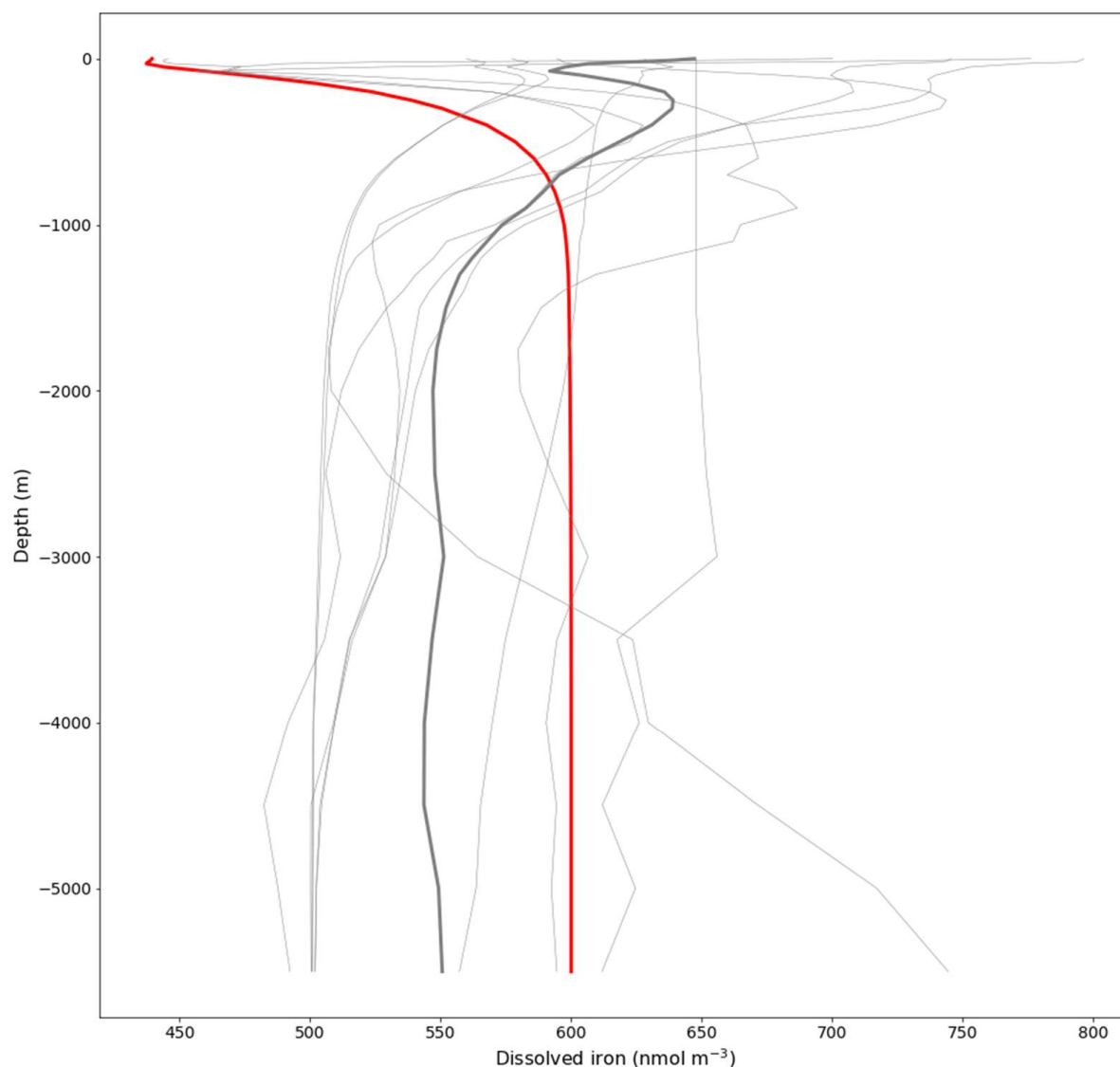
Figure 13 - Global mean depth profiles of dissolved iron concentration for
CanESM5-CanOE and other CMIP6 models that published this field.
GFDL-CM4 is excluded because it has very high concentrations (>2000
nmol m⁻³) near the surface. Thick red line represents CanESM5-CanOE, thin
grey lines individual CMIP6 models, and the thick grey line the model
ensemble mean (excluding CanESM5-CanOE and GFDL-CM4).

544   remineralization) profile, some a more "scavenged-type" (maximal at the surface, declining with

545   depth) profile (cf. Li, 1991; Nozaki, 2001), and others a hybrid profile (increasing downward but

546   with a surface enrichment). CanESM5-CanOE is at the "nutrient-type" end of spectrum with a

547   generally monotonic increase with depth to a near-constant deep-water concentration of 0.6 nM

548   and a very slight near-surface enrichment (see also Supplementary Figures S4b,c). In CanESM5-

549   CanOE the scavenging model is very simple, with distinct regimes for concentrations greater or

550   less than 0.6 nM; scavenging rates are very high above this threshold which causes deep-water

551   concentrations to converge on this value. The generally nutrient-like profile suggest that in

552   CanOE the scavenging rate is quite low for concentrations below 0.6 nM. CanOE considers

553   particulate organic matter (POM) as an index of all particulate matter available for scavenging

554   onto, and model POM concentrations fall off rapidly below the euphotic zone (not shown).

555

556   Mean surface nitrate and dFe concentrations for selected ocean regions are shown in Figure 14.

557   CanESM5-CanOE shows concentrations that are within the range of CMIP6 models, although in

558   some cases at the higher or lower end. Surface nitrate concentrations generally compare

559   favourably with the observation-based climatology, but are biased low in HNLC regions other

560   than the Southern Ocean. These biases are not necessarily a consequence of having too much or

561   too little iron. For example, in the Southern Ocean CanESM5-CanOE has among the highest

562   surface nitrate concentrations, but it also has some of the highest dFe concentrations, and the

563   high nitrate bias is present in CanESM5 as well. Comparisons with the limited GEOTRACES

564   data available suggest that near surface dFe concentrations in the Southern Ocean are biased high

565   rather than low in CanESM5-CanOE (not shown). One region where there does seem to be a

566   strong correlation between surface nitrate and dFe concentrations is the western subarctic
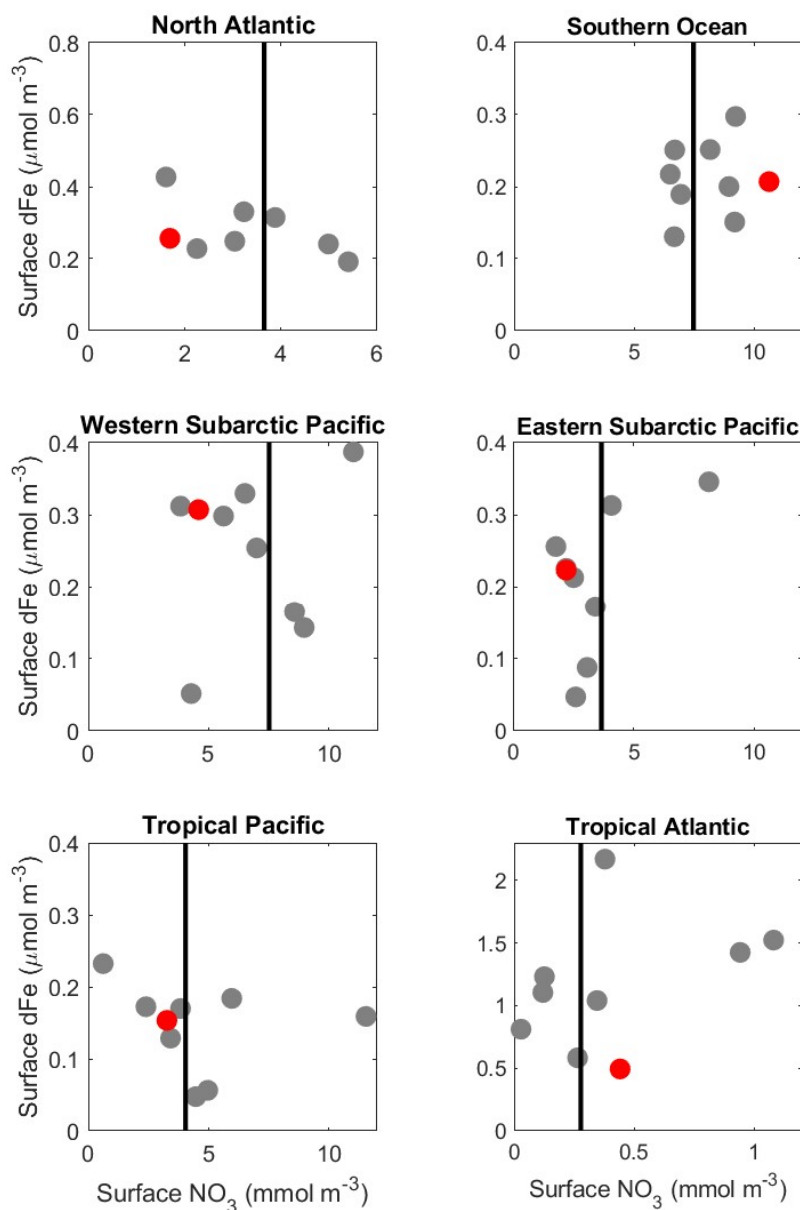
Figure 14 - Mean surface nitrate (NO_3) vs. dissolved iron (dFe) concentrations in different oceans, including the major high nutrient / low chlorophyll (HNLC) regions. CanESM5-CanOE is shown as a red dot and other CMIP5 models as grey dots (CanESM5 is not included because it does not have iron). Observed NO_3 is shown as a vertical black line as there are no observational estimates of dFe concentration. Region definitions are given in Supplementary Table S4.

568   Pacific. All but two models fall along a spectrum from high Fe / low nitrate to low Fe / high

569   nitrate. CanESM5-CanOE falls near the high Fe / low nitrate end of the range.

570

571   Surface nitrate concentrations along the Pacific equator during the upwelling season (June-

572   October) for CanESM5 and CanESM5-CanOE are shown in Figure 15. CanESM5-CanOE better

573   represents the east-west gradient, while CanESM5 has slightly higher concentrations in the core

574   upwelling region. Both models underestimate the highest concentrations around 100°W. Some

575   localized maxima in this data product are due to undersampling; however, examination of

576   ancillary data sets such as satellite sea surface temperature suggests that the enrichment at

577   100°W accurately reflects ocean upwelling (not shown). Although CanESM5 iron limitation is

578   calculated from an earlier version of the same data product, the Fe mask is based on the

579   minimum nitrate concentration over the annual cycle, whereas the data shown here are for the

580   upwelling season. In CanESM5-CanOE, the distribution of surface nitrate is an emergent

581   property of the model, and the fidelity to the observed distribution is generally good.

582

583   **3.4 Plankton biomass, detritus, and particle flux**

584

585   The relative abundance of the four living plankton groups are shown in Figure 16 for a range of

586   ocean regions. Both CanESM models mostly compare favourably with observation-based

587   estimates of phytoplankton biomass, except in the tropics where CanESM5-CanOE has very high

588   biomass. Both CanESM models have low phytoplankton biomass in the North Atlantic. In the

589   North Pacific and the Southern Ocean, CanESM5-CanOE reproduces the observation-based

590   estimates well, and CanESM5 slightly less well. The general pattern is that large and small
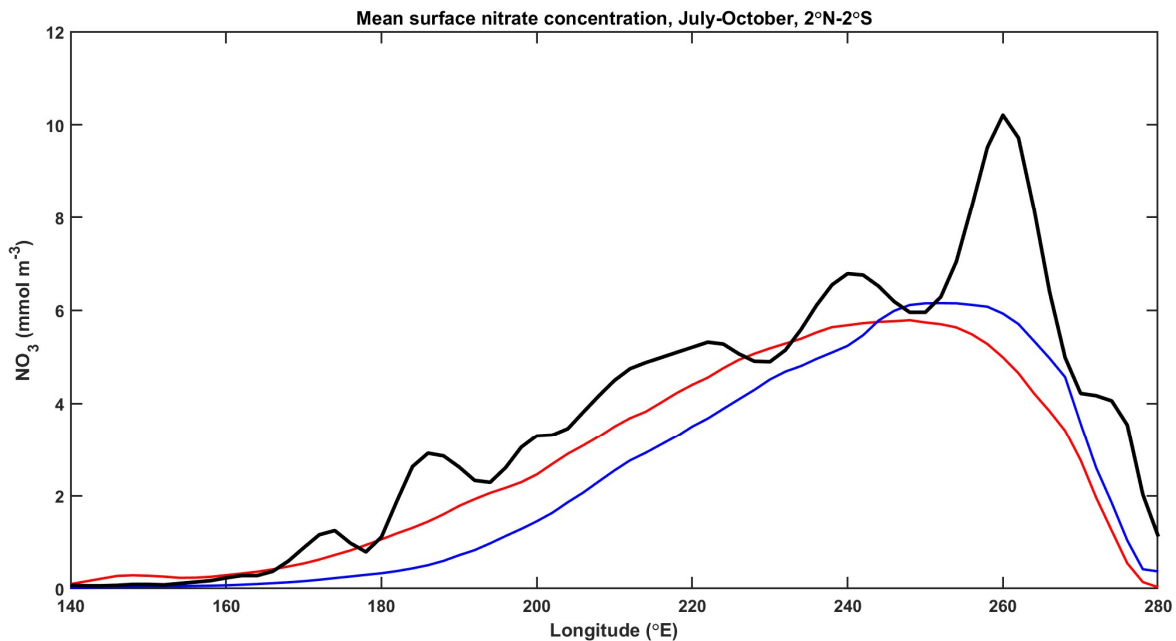
Figure 15 - Surface nitrate (NO3) concentrations along the Pacific equator (mean from 2°S-2°N) during the upwelling season (June-October) for CanESM5-CanOE (red), CanESM5 (blue), and WOA2013 observations (black).
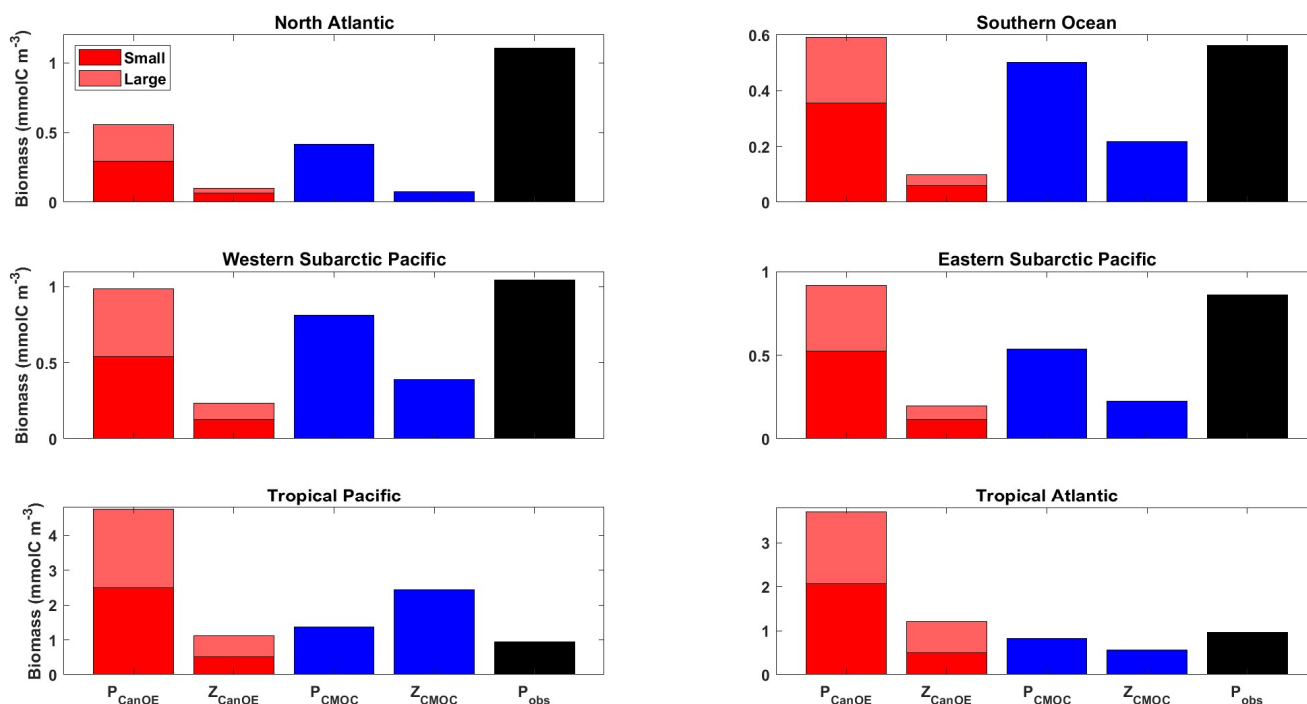
Figure 16 - Annual mean surface ocean concentration of large and small phytoplankton and zooplankton in CanESM5-CanOE (red) and of phytoplankton and zooplankton in CanESM5 (blue) for the representative ocean regions shown in Figure 14. Observational estimates (black) are for phytoplankton biomass calculated from satellite ocean colour estimates of surface chlorophyll (SeaWiFS/MODIS; Tesdal et al. 2016), assuming a carbon-to-chlorophyll ratio of 50 g/g. Region definitions are given in Supplementary Table S4.

593   phytoplankton have similar abundance, and are substantially more abundant than zooplankton.

594   Part of the rationale for multiple food chains is that they better represent the way that actual

595   plankton communities adapt to different physical ocean regimes and therefore are better able to

596   simulate distinct ocean regions with a single parameter set (e.g., Chisholm, 1992; Armstrong,

597   1994; Landry et al., 1997; Friedrichs et al., 2007). The expectation is that small phytoplankton

598   will be more temporally stable and large phytoplankton will fluctuate more strongly between

599   high and low abundances.

600

601   The mean annual cycles of surface chlorophyll largely conform to the expected pattern, e.g., in

602   the North Atlantic and the western subarctic Pacific large phytoplankton are dominant in summer

603   and much more variable over the seasons (Figure 17). Compared to observations, CanESM5

604   models underestimate the amplitude of the seasonal cycle in the North Atlantic and overestimate

605   it in the North Pacific. CanESM5 shows a stronger and earlier North Atlantic spring bloom

606   compared to CanESM5-CanOE; the observations are in between the two in terms of timing, and

607   both models underestimate the amplitude (Figure 17). In the tropics, the seasonal cycle is weak.

608   The tropical Atlantic shows the expected seasonal cycle but not the expected dominance of large

609   phytoplankton in summer. These size-fractionation patterns are difficult to validate against

610   observations. CanESM5-CanOE generally overestimates the total near surface chlorophyll in

611   both the tropical Pacific and the tropical Atlantic.

612

613   Zooplankton biomass (especially microzooplankton) is also somewhat difficult to test against

614   observations, but our model concentrations appear to be biased low. White et al. (1995), for

615   example, show a transect of vertically resolved mesozooplankton abundance along 140°W in the
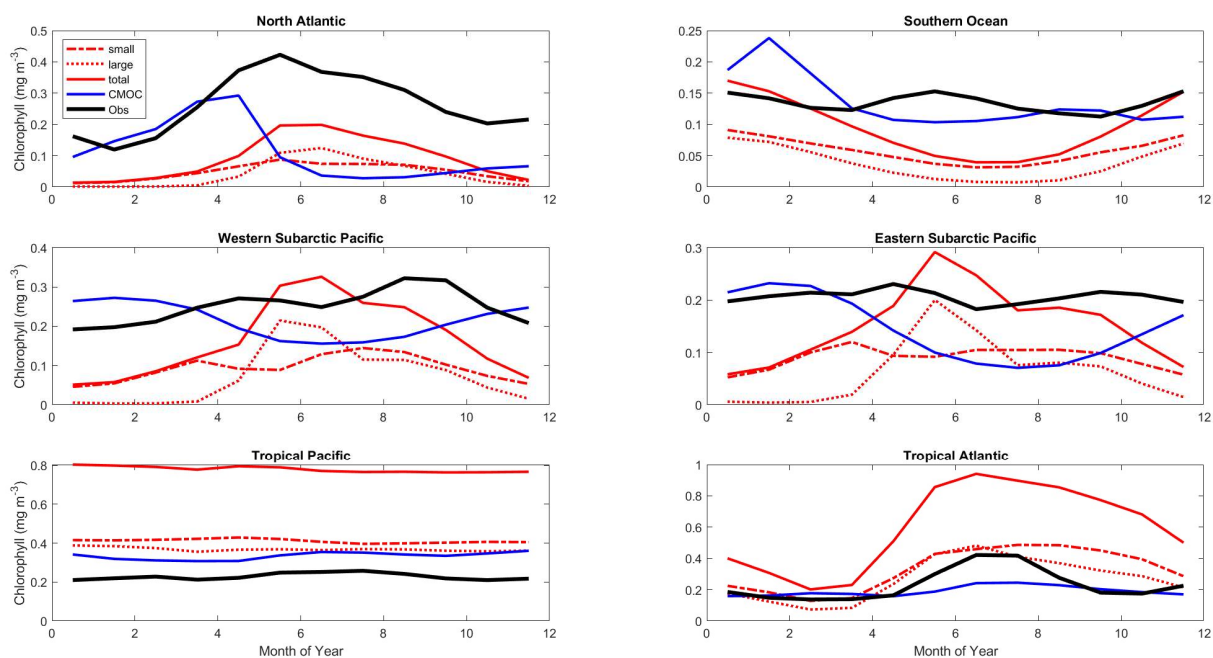
Figure 17 - Mean annual cycle of surface chlorophyll for the representative ocean regions shown in Figures 14 and 16. CanESM5-CanOE large and small phytoplankton concentrations are shown separately and combined (red) along with CanESM5 (blue) and observational estimates (black). Region definitions are shown in Supplementary Table S4.

617   tropical Pacific, with biomass ranging from about 0.1-0.7 mmolC m^3; CanESM5-CanOE

618   concentrations in this region are much lower. Stock et al. (2014) estimated depth-integrated

619   biomass of phytoplankton, mesozooplankton, and microzooplankton for a range of oceanic

620   locations in which intensive field campaigns have occurred (estimates of microzooplankton

621   biomass are relatively sparse). They found that in most locations phytoplankton and (combined)

622   zooplankton biomass are of comparable magnitude, whereas in CanESM5-CanOE zooplankton

623   biomass is consistently lower (Figure 16). The global integral biomass of mesozooplankton is

624   about an order of magnitude less than the 0.19 PgC estimated by Moriarty and O'Brien (2013).

625   The CanESM5 total of 0.14 Pg is relatively close to the Moriarty estimate but implicitly includes

626   microzooplankton.

627

628   Surface chlorophyll and POC for CanESM5-CanOE and for ocean colour observational data are

629   shown in Figure 18 (POC in the model is the sum of phytoplankton, microzooplankton, and

630   detrital carbon). The observations have a lower limit for POC that is not present in the model

631   (~17 mgC m^{-3}), which is unsurprising given the processes neglected in the model, i.e., in regions

632   of very low chlorophyll there is still substantial dissolved organic carbon, bacteria that consume

633   it, and microzooplankton that consume the bacteria and produce particulate detritus. The

634   observational data show a fairly linear relationship at low concentrations, but with a curvature

635   that implies a greater phytoplankton fraction in more eutrophic environments (cf. Chisholm,

636   1992). The model, by contrast, shows a fairly linear relationship over the whole range of

637   concentrations. In other words, the phytoplankton share of POC is higher and more constant in

638   the model than in the observations. The living biomass (phytoplankton + microzooplankton)

639   fraction of total POC in CanOE is generally in excess of 50% (not shown), which is implausible
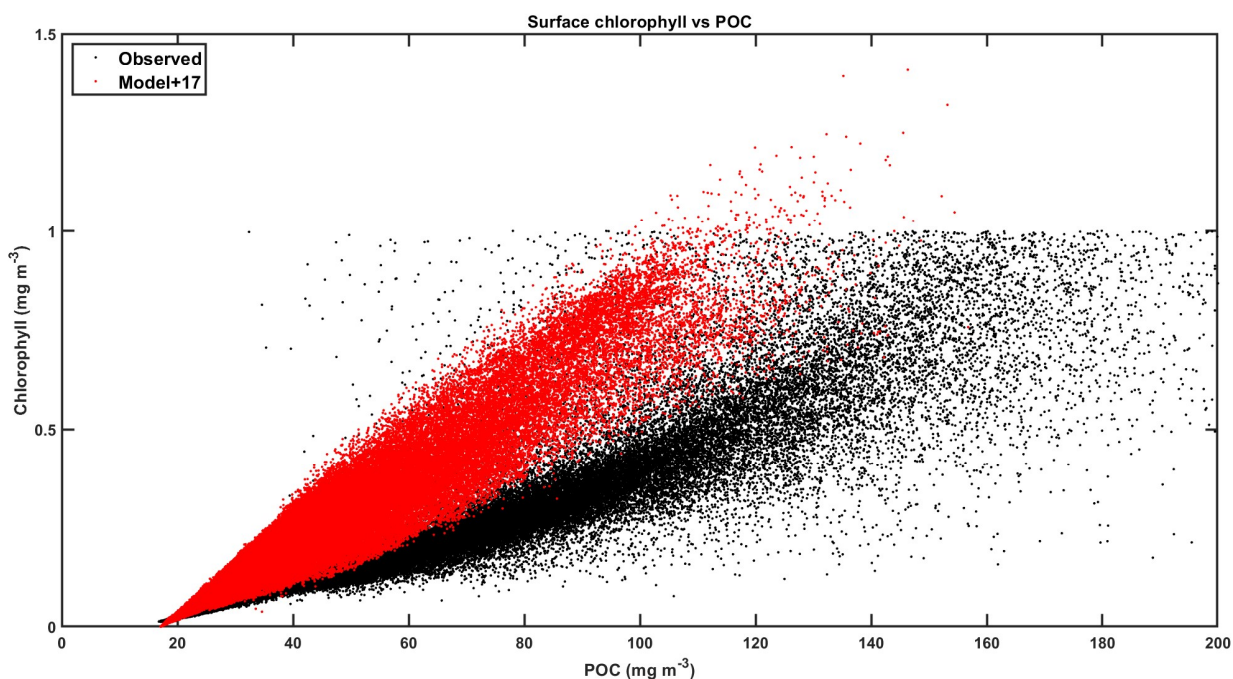
Figure 18 - Climatological surface particulate organic carbon (POC) vs. chlorophyll for CanESM5-CanOE (red) and observations (black). Data are for all ocean grid points (2x2° uniform global grid) for all months of the year where observational data are available. Model POC is offset 17 mg m^{-3} for illustrative purposes.

641   for a real-world oceanic microbial community (e.g., Christian and Karl, 1994) but consistent

642   with the relatively low rates of export from the euphotic zone.

643

644   Export production for a range of CMIP6 models is shown in Figure 19a. CanESM5-CanOE is at

645   the low end of the range. Observations are not shown because the range of observational

646   estimates covers almost the entire range of the plot (e.g., Siegel et al., 2016). Note also that

647   CanESM5 export is quite a bit lower than in CanESM2, which is relatively high for CMIP5

648   models (not shown). The difference between CanESM2 and CanESM5 is attributable primarily

649   to different circulation, although the different initialization fields for nitrate might also play a

650   small role. The lower rate in CanESM5-CanOE is consistent with the above results regarding

651   plankton community structure (e.g., the concentration of detritus is generally low compared to

652   living biomass), as well as the lower sinking rate for small detritus. The latitudinal distribution of

653   export is shown in Figure 19b. CanESM5 shows very high export in the mid-latitudes of the

654   Southern Ocean, similar to CanESM2 (not shown). Both CanESM5 models show latitudinal

655   patterns consistent with the range of other models. CanESM5 has slightly greater export in the

656   equatorial zone; in both CanESM models the equatorial enrichment attenuates very rapidly with

657   latitude and the rates are low in the subtropics.

658

659   **3.5 Historical trends**

660

661   Cumulative ocean uptake of CO_2 is shown in Figure 20 for the historical experiment (1850-

662   2014). CanESM models are biased low relative to observation based estimates (~145 PgC, see

663   Friedlingstein et al., 2020) and the ensemble mean of other models (144 PgC, Figure 20), but fall
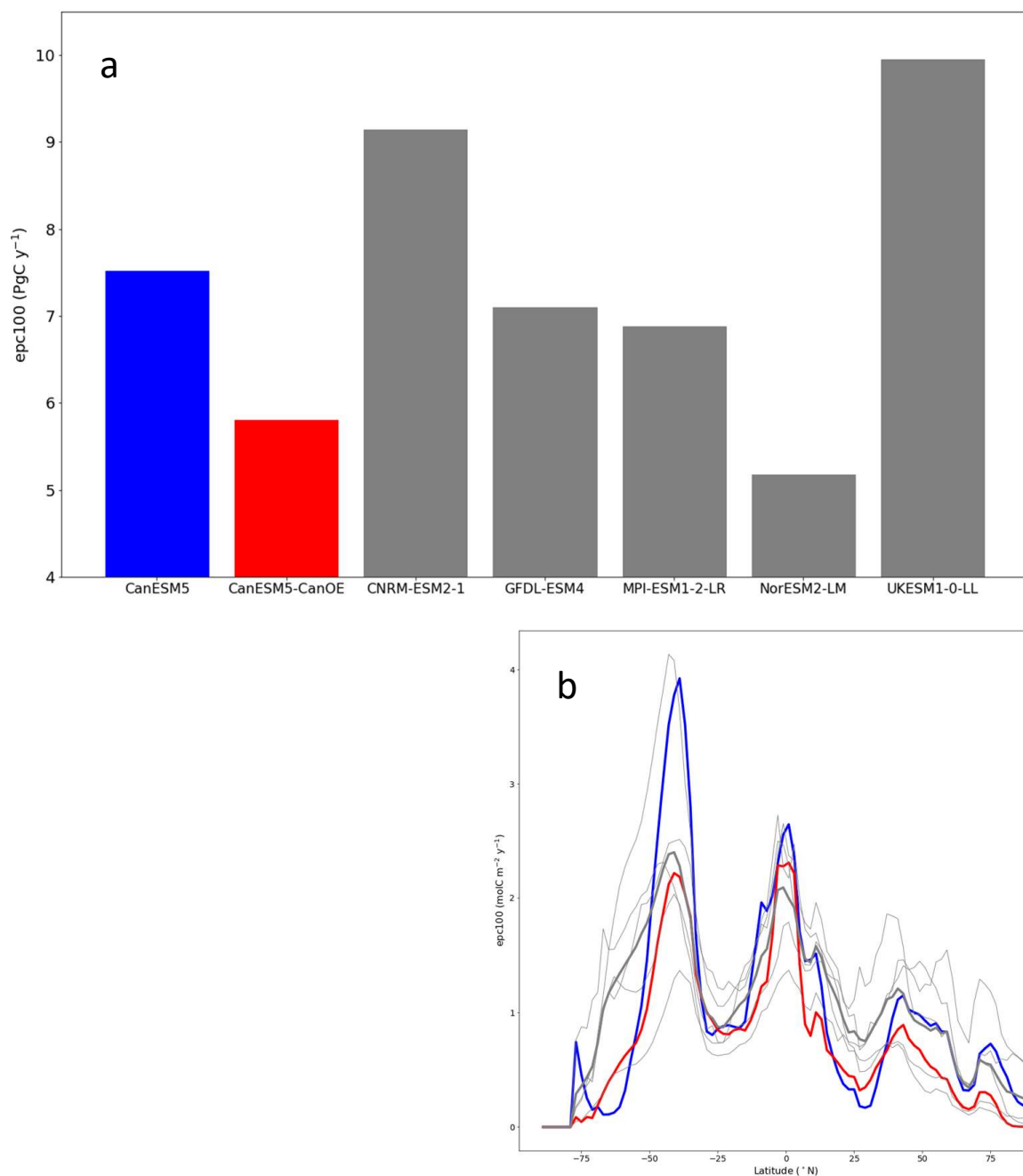
Figure 19 - (a) Global total export production (epc100) in PgC y^{-1} (b) and zonal mean export production in molC m^{-2} y^{-1} according to selected CMIP6 models (mean for 1985-2014 of historical experiment). Thick red line represents CanESM5-CanOE, thick blue line CanESM5, thin grey lines individual CMIP6 models, and thick grey line the model ensemble mean (excluding CanESM5 and CanESM5-CanOE).
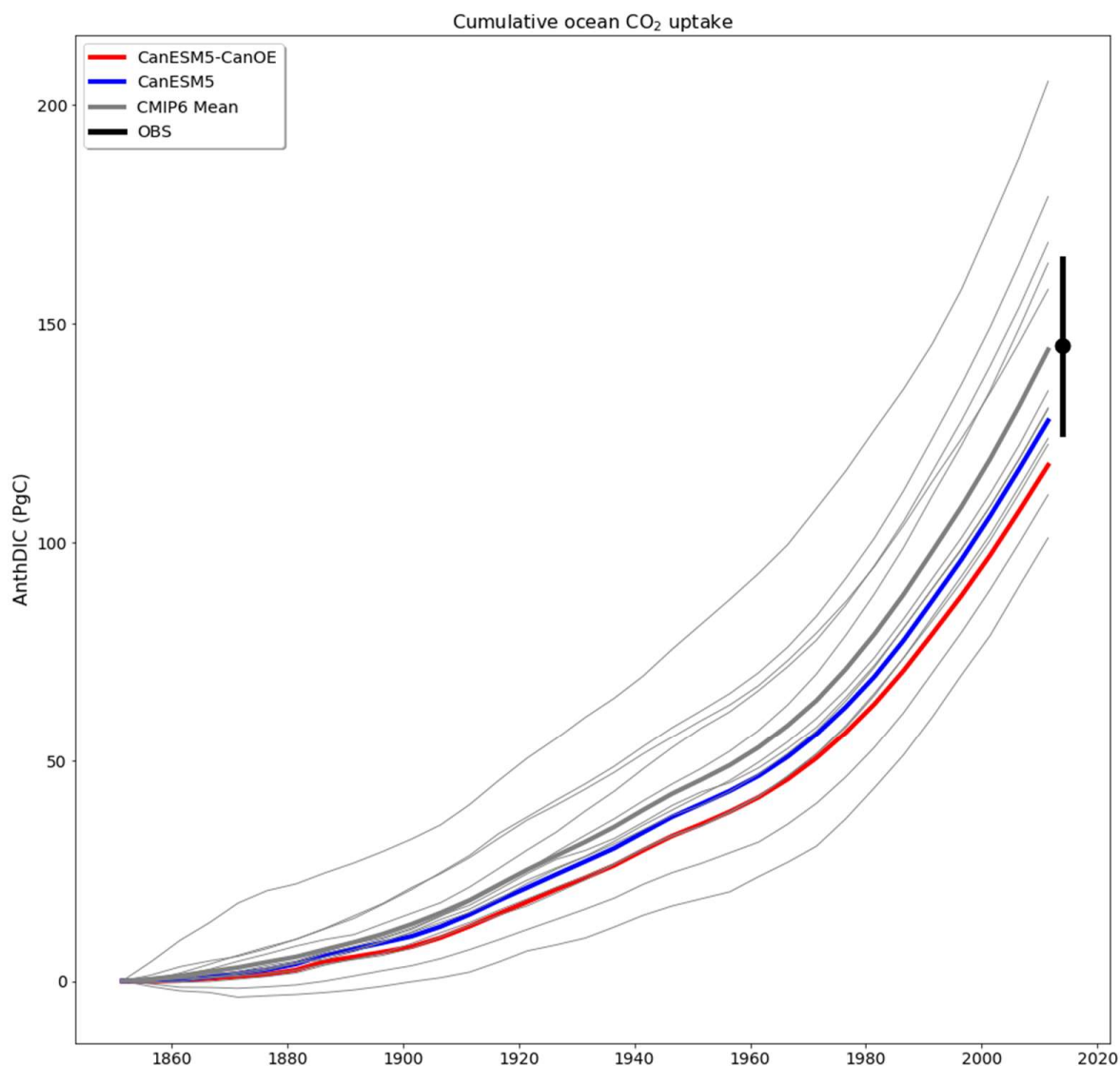
Figure 20 - Cumulative ocean uptake of carbon dioxide (CO_2) as anthropogenic dissolved inorganic carbon (AnthDIC) in PgC over the course of the historical experiment (1850-2014). Data are shown as successive five-year means. CMIP6 mean (thick grey line) indicates ensemble mean for CMIP6 models (thin grey lines) excluding CanESM5 (blue) and CanESM5-CanOE (red). An observation-based estimate of 145±20 PgC (Friedlingstein et al., 2020) is shown for nominal year 2014 (black).

666   well within the spread of CMIP6 models. CanESM5-CanOE has lower cumulative uptake than

667   CanESM5 by ~ 10 PgC. As the models were not fully equilibrated when the historical run was

668   launched, this difference does not necessarily arise from the biogeochemical model structure;

669   part of the difference can be attributed to differences in the spinup protocol (cf. Séférian et al.,

670   2016). The drift in the piControl experiment over the 165 years from the branching off of the

671   historical experiment is -10.5 PgC in CanESM5-CanOE and -5.9 PgC in CanESM5, so drift

672   accounts for about half (44%) of the difference in net ocean CO_2 uptake. The vertical distribution

673   of anthropogenic DIC is very similar between CanESM5 and CanESM5-CanOE (not shown).

674

675   The long-term trend in global total export production is shown in Figure 21. The model values

676   must be normalized in order to compare trends, since the differences among means are large

677   compared to the changes over the historical period (Figure 19). CanESM5 shows a greater

678   decline than most other CMIP6 models, while CanESM5-CanOE is more similar to non-

679   CanESM models. Such trends are difficult or impossible to meaningfully constrain with

680   observations, but the general expectation has been that export will decline somewhat due to

681   increasing stratification (e.g., Steinacher et al., 2010). The change in CanESM5 is geographically

682   widespread and not concentrated in a specific region or regions: export is maximal in the tropics

683   and the northern and southern mid-latitudes (Figure 19b) and declines over the historical period

684   in all of these regions (Supplementary Figure S1). In CanESM5-CanOE, export declines in the

685   same regions, but the magnitude of the change is smaller, and in the Southern Ocean increases

686   and decreases in different latitude bands largely offset each other.
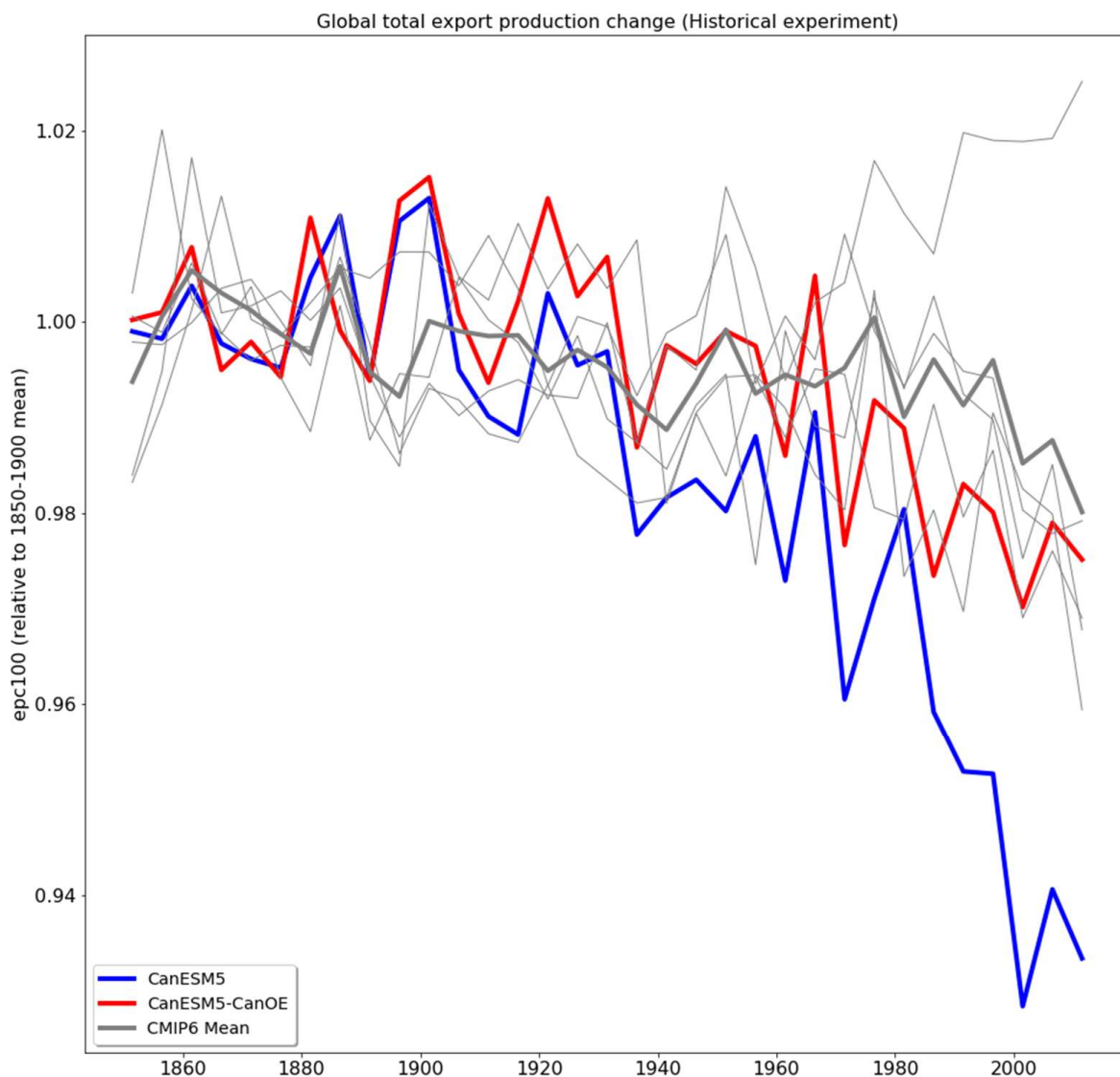
687

688

Figure 21 - Change in export production (epc100) over the course of the historical experiment (1850-2014), normalized to the 1850-1900 mean. Data are shown as successive five-year means. Thick red line represents CanESM5-CanOE, thick blue line CanESM5, thin grey lines other CMIP6 models, and thick grey line the ensemble mean of non-CanESM models.

690   The trend in the volume of ocean water with O_2 concentration less than 6 or 60 mmol m^{-3} is

691   shown in Figure 22. Again, the totals are normalized to a value close to the preindustrial, as the

692   differences among models are large (Figure 5). For the volume with <60 mmol m^{-3}, CanESM

693   models show relatively little change; in CanESM5 the volume actually declines slightly, while in

694   CanESM5-CanOE it increases, but the total change is <1% in each case. As with the baseline

695   volumes, the range among models is large, with one model showing an increase approaching

696   10% of the total volume estimated for WOA2013 (Figures 5b and 22b). For the volume with <6

697   mmol m^{-3} (Figure 22a), CanESM models are among the most stable over time. In CanESM5, the

698   volume again declines, although this is within the range of internal variability. Again some

699   models show fairly large excursions, but in this case none shows a strong secular trend over the

700   last half-century.

701

702   **4. Discussion**

703

704   The development of CanOE was undertaken in response to some of the most severe limitations

705   of CanESM1/2, and in light of our collective experience. In addition to CMOC (Zahariev et al.,

706   2008), previous models developed by members of our group include Denman and Peña (1999;

707   2002), Christian et al. (2002a; 2002b), Christian (2005), and Denman et al. (2006). Christian et

708   al. (2002a) had a prognostic Fe cycle and multiple phytoplankton and zooplankton species, but

709   had fixed elemental ratios. Christian (2005) incorporated a cellular-regulation model, but only

710   for a single species and without Fe limitation. Christian (2005) had prognostic chlorophyll

711   whereas Denman and Pena (1999; 2002) and Christian et al. (2002a) used an irradiance-depend
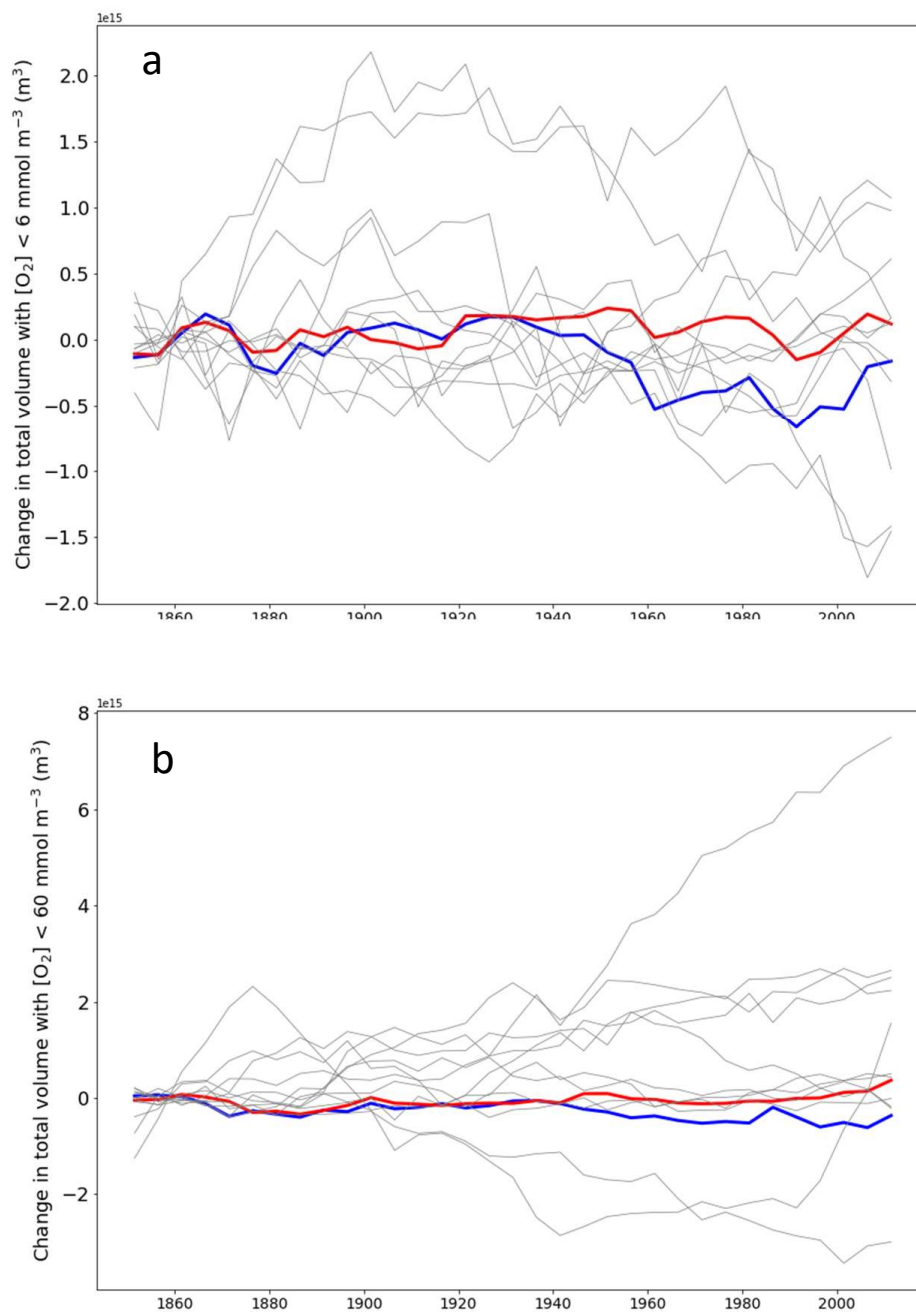
712

Figure 22 - (a) Change in total ocean volume with oxygen (O_2) concentration less than (a) 6 mmol m^{-3} and (b) 60 mmol m^{-3} over the course of the historical experiment (1850-2014), normalized to the 1850-1870 mean. Data are shown as successive five-year means. Thick red line represents CanESM5-CanOE, thick blue line CanESM5, and thin grey lines other CMIP6 models.

714   ent diagnostic formulation. Christian et al. (2002a) used multiplicative (Franks et al., 1986) graz-

715   ing, which creates stability in predator-prey interactions but severely limits phytoplankton bio-

716   mass accumulation under nutrient-replete conditions.

717

718   One of the most important lessons from Christian et al. (2002a; 2002b) was that when a fixed

719   Fe/N ratio is employed, sensitivity to this parameter is extreme. Because Fe cell quotas are far

720   more variable than N, P, or Si quotas, treating this parameter as constant results in the specified

721   value influencing the overall solution far more than any other parameter. CanESM5-CanOE

722   largely succeeded in creating a prognostic Fe-N limitation model that produces HNLC conditions

723   in the expected regions (Figures 10, 11, 14, 15), although surface nitrate concentration is low rel-

724   ative to observation-based estimates in some cases. External Fe sources and scavenging parame-

725   terizations will be revisited and refined in future versions. We note that the aeolian mineral dust

726   deposition field employed here is derived from the CanESM atmosphere model; these processes

727   are not presently interactive but could be made so in the future.

728

729   A particular issue with CanESM2 was that extremely high concentrations of nitrate occurred un-

730   der the Eastern Boundary Current (EBC) upwelling regions. This error resulted from spreading

731   denitrification out over the ocean basin so that introduction of new fixed N from N_2 fixation

732   would balance denitrification losses within each vertical column, whereas in the real world deni-

733   trification is highly localized in the low oxygen environments under the EBCs. CanESM2 did not

734   include oxygen, but CanESM5 CMOC incorporates oxygen as a 'downstream' tracer that does

735   not feed back on other biogeochemical processes. The incorporation of a more process-based de-

736   nitrification parameterization in CanOE is independent of the many other processes that are pre-

737   sent in CanOE but not in CMOC: a CMOC-like model with prognostic denitrification is clearly

738   an option. We chose not to include explicit, oxygen-dependent denitrification in CanESM5 be-

739   cause we wanted to maintain a CMOC-based model as close to the CanESM2 version as possi-

740   ble, and because oxygen would not then be a downstream tracer that does not affect other pro-

741   cesses.

742

743   CanOE for the most part successfully reproduces the overall distribution of major tracers such as

744   nitrate, oxygen, DIC and alkalinity (and dFe, to the extent that its distribution is known). One

745   could argue that the gains made relative to CMOC are incremental. However, it is also important

746   to note that CanOE explicitly simulates important processes that are highly parameterized or

747   specified in CMOC. For example, the maintenance of HNLC regions is hardwired into CMOC

748   by specifying iron limitation as a function of the present-day observed distribution of surface ni-

749   trate. Both models show substantial gains in skill relative to CanESM2. These gains are similar

750   in the two models and in coupled or ocean only (with CanESM2 forcing) mode (not shown) and

751   are, therefore, attributable primarily to improvements in the ocean circulation model, although

752   differences in initialization and spinup may also play a small role (e.g., Séférian et al., 2016).

753

754   Plankton community structure in CanOE is somewhat biased toward high concentrations of phy-

755   toplankton, low concentrations of zooplankton and detritus, and low export (Sect. 3.4). In the de-

756   velopment phase, a fair number of experiments were conducted with various values of the graz-

757   ing rates and detritus sinking speeds. A wide range of values of these parameters was tested, with

758   no resulting improvement in the overall results. Possibly the detrital remineralization rates are

759 too high, although primary production is also on the low end of the CMIP6 range (not shown),

760 and would probably decline further if these rates were decreased. The model was designed

761 around the Armstrong (1994) hypothesis of 'supplementation' vs 'replacement', i.e., small phy-

762 toplankton and their grazers do not become much more abundant in more nutrient-rich environ-

763 ments but rather stay at about the same level and are joined by larger species that are absent in

764 more oligotrophic conditions (see also Chisholm, 1992; Landry et al., 1997; Friedrichs et al.,

765 2007). The results presented here suggest that this was partially achieved but further improve-

766 ment is possible (Figure 17).

767

768 As to whether the gains in skill with CanOE justify the extra computational cost, Taylor dia-

769 grams (Figures 4, 8, 9, and Supplementary Figure S2) show a modest but consistent gain across

770 variables and depths, especially for alkalinity at mid-depths (Supplementary Figure S2), for

771 which CanEM5 displays the least skill relative to other fields or depths. Other processes that are

772 highly parameterized in CMOC, such as calcification and $CaCO_3$ dissolution, were not addressed

773 in detail in this paper, but are an important factor in determining the subsurface distribution of

774 alkalinity. As noted above for maintenance of HNLC conditions, we emphasize that we are simu-

775 lating as an emergent property something that is parameterized in CMOC, and doing at least as

776 well in terms of model skill. As a general rule, the potential for improving skill and achieving

777 better results in novel environments (e.g., topographically complex regional domains like the

778 Arctic Ocean and the boreal marginal seas), is expected to be greater in less parameterized mod-

779 els (e.g., Friedrichs et al., 2007; Tesdal et al., 2016).

780

781   An updated version of CMOC with prognostic denitrification is clearly possible. However, for

782   the reasons discussed above, a prognostic Fe cycle with a fixed phytoplankton Fe/N remains

783   problematic, and the model would still have a single detritus sinking speed and remineralization

784   length scale. We are also developing CanOE for regional downscaling applications (Hayashida,

785   2018; Holdsworth et al., 2021), and it is likely that the simplification of having a single particle

786   sinking speed is not well suited to a domain with complex topography and prominent continental

787   shelf and slope. The number of tracers in CanOE is not particularly large compared with other

788   CMIP6 models. We expect to further refine CanOE and its parameterizations, evaluate it against

789   new and emerging ocean data sets (e.g., GEOTRACES, biogeochemical ARGO), and incremen-

790   tally improve CMOC (which we will maintain for a wide suite of physical-climate experiments

791   for which ocean biogeochemistry is not central to the purpose). For CMIP6, we chose to keep

792   CMOC as close to the CanESM2 version as possible. This strategy allows us to quantify how

793   much of the improvement in model skill is due to the physical circulation, which is in fact sub-

794   stantial (e.g., Figure 8). The CanESM terrestrial carbon model is also undergoing important new

795   developments (e.g., Asaadi and Arora, 2021) and we expect CanESM to continue to offer a cred-

796   ible contribution to global carbon cycle studies, as well as advancing regional downscaling and

797   impacts science.

798

799   *Code availability*. The full CanESM5 source code is publicly available at

800   gitlab.com/cccma/canesm; within this tree the CMOC/CanOE code can be found at

801   gitlab.com/cccma/cannemo/-/tree/v5.0.3/nemo/CONFIG/CCC_CANCPL_ORCA1_LIM_CMOC

802   or CCC_CANCPL_ORCA1_LIM_CANOE (last access: 21 September 2021). The version of the

803   code which can be used to produce all the simulations submitted to CMIP6, and described in this

804   paper, is tagged as v5.0.3 and has the associated DOI: https://doi.org/10.5281/zenodo.3251113

805   (Swart et al., 2019b).

806

807   *Data availability*. All CanESM5 simulations conducted for CMIP6, including those described in

808   this paper, are publicly available via the Earth System Grid Federation (ESGF). All observational

809   data and other CMIP6 model data used are publicly available.

810

811   *Author contributions.* Formulation of the overall research goals and aims: JRC, KLD, NS, NCS;

812   Implementation and testing of the model code: JRC, HH, AMH, WGL, OGJR, AES, NCS; Car-

813   rying out the experiments: JRC, WGL, OGJR, AES, NCS; Creation of the published work: JRC,

814   HH, AMH, AES, NS, NCS.

815

816   *Competing interests*. The authors declare that they have no conflict of interest.

817

818   *Disclaimer*. CanESM has been customized to run on the ECCC high-performance computer, and

819   a significant fraction of the software infrastructure used to run the model is specific to the indi-

820   vidual machines and architecture. While we publicly provide the code, we cannot provide any

821   support for migrating the model to different machines or architectures.

822

Geoscientific
Model Development
Discussions

826   data contributors. The Python packages mocsy by Jim Orr and SkillMetrics by Peter Rochford

827   were invaluable tools in the analysis. William Merryfield and Andrew Ross made useful com-

828   ments on an earlier draft. This paper is dedicated to the memory of Mr. Fouad Majaess, who sup-

829   ported CCCMa supercomputer users for many years and passed away suddenly in 2020.

830
831
832   **Literature Cited**
833
834

835   Arguez, A. and Vose, R.: The Definition of the Standard WMO Climate Normal The Key to
836   Deriving Alternative Climate Normals, Bulletin of the American Meteorological Society, 92,
837   699-704, 10.1175/2010BAMS2955.1, 2011.

838

839   Armstrong, R.: Grazing limitation and nutrient limitation in marine ecosystems - steady-state
840   solutions of an ecosystem model with multiple food-chains, Limnology and Oceanography, 39,
841   597-608, 1994.

842

843   Arora, V., Scinocca, J., Boer, G., Christian, J., Denman, K., Flato, G., Kharin, V., Lee, W., and
844   Merryfield, W.: Carbon emission limits required to satisfy future representative concentration
845   pathways of greenhouse gases, Geophysical Research Letters, 38, 10.1029/2010GL046270,
846   2011.

847

848   Arora, V., Boer, G., Christian, J., Curry, C., Denman, K., Zahariev, K., Flato, G., Scinocca, J.,
849   Merryfield, W., and Lee, W.: The Effect of Terrestrial Photosynthesis Down Regulation on the
850   Twentieth-Century Carbon Budget Simulated with the CCCma Earth System Model, Journal of
851   Climate, 22, 6066-6088, 10.1175/2009JCLI3037.1, 2009.

852

853   Asaadi, A. and Arora, V.: Implementation of nitrogen cycle in the CLASSIC land model,
854   Biogeosciences, 18, 669-706, 10.5194/bg-18-669-2021, 2021.

855

856   Aumont, O., Ethe, C., Tagliabue, A., Bopp, L., and Gehlen, M.: PISCES-v2: an ocean
857   biogeochemical model for carbon and ecosystem studies, Geoscientific Model Development, 8,
858   2465-2513, 10.5194/gmd-8-2465-2015, 2015.

859

860   Babbin, A., Keil, R., Devol, A., and Ward, B.: Organic Matter Stoichiometry, Flux, and Oxygen
861   Control Nitrogen Loss in the Ocean, Science, 344, 406-408, 10.1126/science.1248364, 2014.

862

863   Chisholm, S.W.: Phytoplankton size, in: Primary productivity and biogeochemical cycles in the
864   sea, edited by: Falkowski, P.G., and Woodhead A.D., Plenum, New York, 213-237, 1992.

865

866   Christian, J.: Biogeochemical cycling in the oligotrophic ocean: Redfield and non-Redfield
867   models, Limnology and Oceanography, 50, 646-657, 2005.

868

869 Christian, J. and Karl, D.: Microbial community structure at the United States Joint Global
870 Ocean Flux Study Station ALOHA - inverse methods for estimating biochemical indicator ratios,
871 Journal of Geophysical Research-Oceans, 99, 14269-14276, 10.1029/94JC00681, 1994.

872

873 Christian, J., Arora, V., Boer, G., Curry, C., Zahariev, K., Denman, K., Flato, G., Lee, W.,
874 Merryfield, W., Roulet, N., and Scinocca, J.: The global carbon cycle in the Canadian Earth
875 system model (CanESM1): Preindustrial control simulation, Journal of Geophysical Research-
876 Biogeosciences, 115, 10.1029/2008JG000920, 2010.

877

878 Christian, J. R., Verschell, M. A., Murtugudde, R., Busalacchi, A. J., and McClain, C. R.:
879 Biogeochemical modelling of the tropical Pacific Ocean. I: Seasonal and interannual variability,
880 Deep-Sea Research Part II-Topical Studies in Oceanography, 49, 509-543, 2002a.

881

882 Christian, J. R., Verschell, M. A., Murtugudde, R., Busalacchi, A. J., and McClain, C. R.:
883 Biogeochemical modelling of the tropical Pacific Ocean. II: Iron biogeochemistry, Deep-Sea
884 Research Part II-Topical Studies in Oceanography, 49, 545-565, 0.1016/s0967-0645(01)00111-4,
885 2002b.

886

887 Denman, K. and Pena, M.: A coupled 1-D biological/physical model of the northeast subarctic
888 Pacific Ocean with iron limitation, Deep-Sea Research Part II-Topical Studies in Oceanography,
889 46, 2877-2908, 10.1016/S0967-0645(99)00087-9, 1999.

890

891 Denman, K. and Pena, M.: The response of two coupled one-dimensional mixed layer/planktonic
892 ecosystem models to climate change in the NE subarctic Pacific Ocean, Deep-Sea Research Part
893 II-Topical Studies in Oceanography, 49, 5739-5757, 10.1016/S0967-0645(02)00212-6, 2002.

894

895 Denman, K., Voelker, C., Pena, M., and Rivkin, R.: Modelling the ecosystem response to iron
896 fertilization in the subarctic NE Pacific: The influence of grazing, and Si and N cycling on CO_2
897 drawdown, Deep-Sea Research Part II-Topical Studies in Oceanography, 53, 2327-2352,
898 10.1016/j.dsr2.2006.05.026, 2006.

899

900 Devol, A.H.: Denitrification including anammox, in: Nitrogen in the Marine Environment, 2nd
901 edition, edited by: Capone, D.G., Bronk D.A., Mulholland M.R., and Carpenter E.J., Elsevier,
902 Amsterdam, 263-301, 2008.

903

904 Dickson, A.G., Sabine, C.L., and Christian, J.R., eds.: Guide to best practices for ocean CO_2
905 measurements, PICES Special Publication #3, 2007

906

907 Elser, J. and Urabe, J.: The stoichiometry of consumer-driven nutrient recycling: Theory,
908 observations, and consequences, Ecology, 80, 735-751, 10.1890/0012-
909 9658(1999)080[0735:TSOCDN]2.0.CO;2, 1999.

910

911 Franks, P., Wroblewski, J., and Flierl, G.: Behavior of a simple plankton model with food-level
912 acclimation by herbivores, Marine Biology, 91, 121-129, 10.1007/BF00397577, 1986.

913

Geoscientific
Model Development
Discussions

914   Friedlingstein, P., O'Sullivan, M., Jones, M., Andrew, R., Hauck, J., Olsen, A., Peters, G., Peters,
915   W., Pongratz, J., Sitch, S., Le Quere, C., Canadell, J., Ciais, P., Jackson, R., Alin, S., Aragao, L.,
916   Arneth, A., Arora, V., Bates, N., Becker, M., Benoit-Cattin, A., Bittig, H., Bopp, L., Bultan, S.,
917   Chandra, N., Chevallier, F., Chini, L., Evans, W., Florentie, L., Forster, P., Gasser, T., Gehlen,
918   M., Gilfillan, D., Gkritzalis, T., Gregor, L., Gruber, N., Harris, I., Hartung, K., Haverd, V.,
919   Houghton, R., Ilyina, T., Jain, A., Joetzjer, E., Kadono, K., Kato, E., Kitidis, V., Korsbakken, J.,
920   Landschutzer, P., Lefevre, N., Lenton, A., Lienert, S., Liu, Z., Lombardozzi, D., Marland, G.,
921   Metzl, N., Munro, D., Nabel, J., Nakaoka, S., Niwa, Y., O'Brien, K., Ono, T., Palmer, P., Pierrot,
922   D., Poulter, B., Resplandy, L., Robertson, E., Rodenbeck, C., Schwinger, J., Seferian, R.,
923   Skjelvan, I., Smith, A., Sutton, A., Tanhua, T., Tans, P., Tian, H., Tilbrook, B., Van der Werf,
924   G., Vuichard, N., Walker, A., Wanninkhof, R., Watson, A., Willis, D., Wiltshire, A., Yuan, W.,
925   Yue, X., and Zaehle, S.: Global Carbon Budget 2020, Earth System Science Data, 12, 3269-
926   3340, 10.5194/essd-12-3269-2020, 2020.
927
928   Friedrichs, M., Dusenberry, J., Anderson, L., Armstrong, R., Chai, F., Christian, J., Doney, S.,
929   Dunne, J., Fujii, M., Hood, R., McGillicuddy, D., Moore, J., Schartau, M., Spitz, Y., and
930   Wiggert, J.: Assessment of skill and portability in regional marine biogeochemical models: Role
931   of multiple planktonic groups, Journal of Geophysical Research-Oceans, 112,
932   10.1029/2006JC003852, 2007.
933
934   Garcia, H.E., Locarnini, R.A., Boyer, T.P., Antonov, J.I., Baranova, O.K., Zweng, M.M.,
935   Reagan, J.R., and Johnson, D.R.: World Ocean Atlas 2013, Volume 3: Dissolved Oxygen,
936   Apparent Oxygen Utilization, and Oxygen Saturation. S. Levitus, Ed., A. Mishonov Technical
937   Ed., NOAA Atlas NESDIS 75, 27 pp., 2014.
938
939   Garcia, H.E., Locarnini, R.A., Boyer, T.P., Antonov, J.I., Baranova, O.K., Zweng, M.M.,
940   Reagan, J.R., and Johnson, D.R.: World Ocean Atlas 2013, Volume 4: Dissolved Inorganic
941   Nutrients (phosphate, nitrate, silicate). S. Levitus, Ed., A. Mishonov Technical Ed.; NOAA Atlas
942   NESDIS 76, 25 pp., 2014.
943
944   Geider, R., MacIntyre, H., and Kana, T.: A dynamic regulatory model of phytoplanktonic
945   acclimation to light, nutrients, and temperature, Limnology and Oceanography, 43, 679-694,
946   1998.
947
948   Guilyardi, E. and Madec, G.: Performance of the OPA/ARPEGE-T21 global ocean-atmosphere
949   coupled model, Climate Dynamics, 13, 149-165, 10.1007/s003820050157, 1997.
950
951   Hayashida, H.: Modelling sea-ice and oceanic dimethylsulde production and emissions in the
952   Arctic, PhD thesis, University of Victoria, 2018.
953
954   Holdsworth, A.M., Zhai, L., Lu, Y., and Christian, J.R.: Future changes in oceanography and
955   biogeochemistry along the Canadian Pacific continental margin, Frontiers in Marine Science,
956   10.3389/fmars.2021.602991, 2021.
957
958   Jetten, M., Wagner, M., Fuerst, J., van Loosdrecht, M., Kuenen, G., and Strous, M.:
959   Microbiology and application of the anaerobic ammonium oxidation ('anammox') process,

960   Current Opinion in Biotechnology, 12, 283-288, 10.1016/S0958-1669(00)00211-1, 2001.
961
962   Johnson, K. S., Gordon, R. M., and Coale, K. H.: What controls dissolved iron concentrations in
963   the world ocean?, Marine Chemistry, 57, 137-161, 10.1016/s0304-4203(97)00043-1, 1997.
964
965   Johnson, K., Elrod, V., Fitzwater, S., Plant, J., Chavez, F., Tanner, S., Gordon, R., Westphal, D.,
966   Perry, K., Wu, J., and Karl, D.: Surface ocean-lower atmosphere interactions in the Northeast
967   Pacific Ocean Gyre: Aerosols, iron, and the ecosystem response, Global Biogeochemical Cycles,
968   17, 10.1029/2002GB002004, 2003.
969
970   Lambert, S. and Boer, G.: CMIP1 evaluation and intercomparison of coupled climate models,
971   Climate Dynamics, 17, 83-106, 10.1007/PL00013736, 2001.
972
973   Landry, M., Barber, R., Bidigare, R., Chai, F., Coale, K., Dam, H., Lewis, M., Lindley, S.,
974   McCarthy, J., Roman, M., Stoecker, D., Verity, P., and White, J.: Iron and grazing constraints on
975   primary production in the central equatorial Pacific: An EqPac synthesis, Limnology and
976   Oceanography, 42, 405-418, 10.4319/lo.1997.42.3.0405, 1997.
977
978   Lauvset, S., Key, R., Olsen, A., van Heuven, S., Velo, A., Lin, X., Schirnick, C., Kozyr, A.,
979   Tanhua, T., Hoppema, M., Jutterstrom, S., Steinfeldt, R., Jeansson, E., Ishii, M., Perez, F.,
980   Suzuki, T., and Watelet, S.: A new global interior ocean mapped climatology: the 1 degrees x 1
981   degrees GLODAP version 2, Earth System Science Data, 8, 325-340, 10.5194/essd-8-325-2016,
982   2016.
983
984   Li, Y.: Distribution patterns of the elements in the ocean - a synthesis, Geochimica et
985   Cosmochimica Acta, 55, 3223-3240, 1991.
986
987   Locarnini, R.A., Mishonov, A.V., Antonov, J.I., Boyer, T.P., Garcia, H.E., Baranova, O.K.,
988   Zweng, M.M., Paver, C.R., Reagan, J.R., Johnson, D.R., Hamilton, M., and Seidov, D.: World
989   Ocean Atlas 2013, Volume 1: Temperature. S. Levitus, Ed., A. Mishonov Technical Ed., NOAA
990   Atlas NESDIS 73, 40 pp., 2013.
991
992   Loladze, I., Kuang, Y., and Elser, J.: Stoichiometry in producer-grazer systems: Linking energy
993   flow with element cycling, Bulletin of Mathematical Biology, 62, 1137-1162,
994   10.1006/bulm.2000.0201, 2000.
995
996   Madec, G. and Imbard, M.: A global ocean mesh to overcome the North Pole singularity,
997   Climate Dynamics, 12, 381-388, 10.1007/s003820050115, 1996.
998
999   Moriarty, R. and O'Brien, T.: Distribution of mesozooplankton biomass in the global ocean,
1000 Earth System Science Data, 5, 45-55, 10.5194/essd-5-45-2013, 2013.
1001
1002 Nozaki, Y.: Elemental Distribution, in: Encyclopedia of Ocean Sciences, edited by: Steele, J.H.,
1003 Thorpe, S.A., and Turekian, K.K., Academic, San Diego, 840-845, 10.1006/rwos.2001.0402,
1004 2001.
1005

1006   Orr, J. C., Najjar, R. G., Aumont, O., Bopp, L., Bullister, J. L., Danabasoglu, G., Doney, S. C.,
1007   Dunne, J. P., Dutay, J. C., Graven, H., Griffies, S. M., John, J. G., Joos, F., Levin, I., Lindsay,
1008   K., Matear, R. J., McKinley, G. A., Mouchet, A., Oschlies, A., Romanou, A., Schlitzer, R.,
1009   Tagliabue, A., Tanhua, T., and Yool, A.: Biogeochemical protocols and diagnostics for the
1010   CMIP6 Ocean Model Intercomparison Project (OMIP), Geoscientific Model Development, 10,
1011   2169-2199, 10.5194/gmd-10-2169-2017, 2017.
1012
1013   Philander, S.G. and Chao, Y.: On the contrast between the seasonal cycles of the equatorial
1014   Atlantic and Pacific oceans, Journal of Physical Oceanography, 21, 1399-1406, 1991.
1015
1016   Raven, J. and Geider, R.: Temperature and algal growth, New Phytologist, 110, 441-461,
1017   10.1111/j.1469-8137.1988.tb00282.x, 1988.
1018
1019   Riche, O. and Christian, J.: Ocean dinitrogen fixation and its potential effects on ocean primary
1020   production in Earth system model simulations of anthropogenic warming, Elementa-Science of
1021   the Anthropocene, 6, 10.1525/elementa.277, 2018.
1022
1023   Schlitzer, R., Anderson, R., Dodas, E., Lohan, M., Geibere, W., Tagliabue, A., Bowie, A.,
1024   Jeandel, C., Maldonado, M., Landing, W., Cockwell, D., Abadie, C., Abouchami, W.,
1025   Achterberg, E., Agather, A., Aguliar-Islas, A., van Aken, H., Andersen, M., Archer, C., Auro,
1026   M., de Baar, H., Baars, O., Baker, A., Bakker, K., Basak, C., Baskaran, M., Bates, N., Bauch, D.,
1027   van Beek, P., Behrens, M., Black, E., Bluhm, K., Bopp, L., Bouman, H., Bowman, K., Bown, J.,
1028   Boyd, P., Boye, M., Boyle, E., Branellec, P., Bridgestock, L., Brissebrat, G., Browning, T.,
1029   Bruland, K., Brumsack, H., Brzezinski, M., Buck, C., Buck, K., Buesseler, K., Bull, A., Butler,
1030   E., Cai, P., Mor, P., Cardinal, D., Carlson, C., Carrasco, G., Casacuberta, N., Casciotti, K.,
1031   Castrillejo, M., Chamizo, E., Chance, R., Charette, M., Chaves, J., Cheng, H., Chever, F.,
1032   Christl, M., Church, T., Closset, I., Colman, A., Conway, T., Cossa, D., Croot, P., Cullen, J.,
1033   Cutter, G., Daniels, C., Dehairs, F., Deng, F., Dieu, H., Duggan, B., Dulaquais, G.,
1034   Dumousseaud, C., Echegoyen-Sanz, Y., Edwards, R., Ellwood, M., Fahrbach, E., Fitzsimmons,
1035   J., Flegal, A., Fleisher, M., van de Flierdt, T., Frank, M., Friedrich, J., Fripiat, F., Frollje, H.,
1036   Galer, S., Gamo, T., Ganeshram, R., Garcia-Orellana, J., Garcia-Solsona, E., Gault-Ringold, M.,
1037   George, E., Gerringa, L., Gilbert, M., Godoy, J., Goldstein, S., Gonzalez, S., Grissom, K.,
1038   Hammerschmidt, C., Hartman, A., Hassler, C., Hathorne, E., Hatta, M., Hawco, N., Hayes, C.,
1039   Heimburger, L., Helgoe, J., Heller, M., Henderson, G., Henderson, P., van Heuven, S., Ho, P.,
1040   Horner, T., Hsieh, Y., Huang, K., Humphreys, M., Isshiki, K., Jacquot, J., Janssen, D., Jenkins,
1041   W., John, S., Jones, E., Jones, J., Kadko, D., Kayser, R., Kenna, T., Khondoker, R., Kim, T.,
1042   Kipp, L., Klar, J., Klunder, M., Kretschmer, S., Kumamoto, Y., Laan, P., Labatut, M., Lacan, F.,
1043   Lam, P., Lambelet, M., Lamborg, C., Le Moigne, F., Le Roy, E., Lechtenfeld, O., Lee, J.,
1044   Lherminier, P., Little, S., Lopez-Lora, M., Lu, Y., Masque, P., Mawji, E., Mcclain, C., Measures,
1045   C., Mehic, S., Menzel Barraqueta, J., van der Merwe, P., Middag, R., Mieruch, S., Milne, A.,
1046   Minami, T., Moffett, J., Moncoiffe, G., Moore, W., Morris, P., Morton, P., Nakaguchi, Y.,
1047   Nakayama, N., Niedermiller, J., Nishioka, J., Nishiuchi, A., Noble, A., Obata, H., Ober, S.,
1048   Ohnemus, D., van Ooijen, J., O'Sullivan, J., Owens, S., Pahnke, K., Paul, M., Pavia, F., Pena, L.,
1049   Petersh, B., Planchon, F., Planquette, H., Pradoux, C., Puigcorbe, V., Quay, P., Queroue, F.,
1050   Radic, A., Rauschenberg, S., Rehkamper, M., Rember, R., Remenyi, T., Resing, J., Rickli, J.,
1051   Rigaud, S., Rijkenberg, M., Rintoul, S., Robinson, L., Roca-Marti, M., Rodellas, V., Roeske, T.,

Rolison, J., Rosenberg, M., Roshan, S., van der Loaff, M., Ryabenko, E., Saito, M., Salt, L., Sanial, V., Sarthou, G., Schallenberg, C., Schauer, U., Scher, H., Schlosser, C., Schnetger, B., Scott, P., Sedwick, P., Semiletov, I., Shelley, R., Sherrell, R., Shiller, A., Sigman, D., Singh, S., Slagter, H., Slater, E., Smethie, W., Snaith, H., Sohrin, Y., Sohst, B., Sonke, J., Speich, S., Steinfeldt, R., Stewart, G., Stichel, T., Stirling, C., Stutsman, J., Swarr, G., Swift, J., Thomas, A., Thorne, K., Till, C., Till, R., Townsend, A., Townsend, E., Tuerena, R., Twining, B., Vance, D., Velazquez, S., Venchiarutti, C., Villa-Alfageme, M., Vivancos, S., Voelker, A., Wake, B., Warner, M., Watson, R., van Weerlee, E., Weigand, M., Weinstein, Y., Weiss, D., Wisotzki, A., Woodward, E., Wu, J., Wu, Y., Wuttig, K., Wyatt, N., Xiang, Y., Xie, R., Xue, Z., Yoshikawa, H., Zhang, J., Zhang, P., Zhao, Y., Zheng, L., Zheng, X., Zieringer, M., Zimmer, L., Ziveri, P., Zunino, P., and Zurbrick, C.: The GEOTRACES Intermediate Data Product 2017, Chemical Geology, 493, 210-223, 10.1016/j.chemgeo.2018.05.040, 2018.

Séférian, R., Gehlen, M., Bopp, L., Resplandy, L., Orr, J., Marti, O., Dunne, J., Christian, J., Doney, S., Ilyina, T., Lindsay, K., Halloran, P., Heinze, C., Segschneider, J., Tjiputra, J., Aumont, O., and Romanou, A.: Inconsistent strategies to spin up models in CMIP5: implications for ocean biogeochemical model performance assessment, Geoscientific Model Development, 9, 1827-1851, 10.5194/gmd-9-1827-2016, 2016.

Siegel, D., Buesseler, K., Behrenfeld, M., Benitez-Nelson, C., Boss, E., Brzezinski, M., Burd, A., Carlson, C., D'Asaro, E., Doney, S., Perry, M., Stanley, R., and Steinberg, D.: Prediction of the Export and Fate of Global Ocean Net Primary Production: The EXPORTS Science Plan, Frontiers in Marine Science, 3, 10.3389/fmars.2016.00022, 2016.

Steinacher, M., Joos, F., Frolicher, T., Bopp, L., Cadule, P., Cocco, V., Doney, S., Gehlen, M., Lindsay, K., Moore, J., Schneider, B., and Segschneider, J.: Projected 21st century decrease in marine productivity: a multi-model analysis, Biogeosciences, 7, 979-1005, 10.5194/bg-7-979-2010, 2010.

Stramski, D., Reynolds, R., Babin, M., Kaczmarek, S., Lewis, M., Rottgers, R., Sciandra, A., Stramska, M., Twardowski, M., Franz, B., and Claustre, H.: Relationships between the surface concentration of particulate organic carbon and optical properties in the eastern South Pacific and eastern Atlantic Oceans, Biogeosciences, 5, 171-201, 10.5194/bg-5-171-2008, 2008.

Strous, M., Heijnen, J., Kuenen, J., and Jetten, M.: The sequencing batch reactor as a powerful tool for the study of slowly growing anaerobic ammonium-oxidizing microorganisms, Applied Microbiology and Biotechnology, 50, 589-596, 10.1007/s002530051340, 1998.

Swart, N., Cole, J., Kharin, V., Lazare, M., Scinocca, J., Gillett, N., Anstey, J., Arora, V., Christian, J., Hanna, S., Jiao, Y., Lee, W., Majaess, F., Saenko, O., Seiler, C., Seinen, C., Shao, A., Sigmond, M., Solheim, L., von Salzen, K., Yang, D., and Winter, B.: The Canadian Earth System Model version 5 (CanESM5.0.3), Geoscientific Model Development, 12, 4823-4873, 10.5194/gmd-12-4823-2019, 2019a.

Swart, N. C., Cole, J., Kharin, S., Lazare, M., Scinocca, J., Gillett, N., Anstey, J., Arora, V., Christian, J., Hanna, S., Jiao, Y., Lee, W., Majaess, F., Saenko, O., Seiler, C., Seinen, C.,

1098 Shao, A., Solheim, L., von Salzen, K., Yang, D., and Winter, B.: The Canadian Earth System
1099 Model (CanESM), v5.0.3., https://doi.org/10.5281/zenodo.3251114, 2019b.
1100
1101 Takeda, S., Chai, F., and Nishioka, J., Eds.: Report of Working Group 22 on Iron Supply and its
1102 Impact on Biogeochemistry and Ecosystems in the North Pacific Ocean. PICES Sci. Rep. No.
1103 42, 60 pp., 2013.
1104
1105 Taylor, K.: Summarizing multiple aspects of model performance in a single diagram., Journal of
1106 Geophysical Research-Atmospheres, 106, 7183-7192, 10.1029/2000JD900719, 2001.
1107
1108 Tesdal, J., Christian, J., Monahan, A., and von Salzen, K.: Evaluation of diverse approaches for
1109 estimating sea-surface DMS concentration and air-sea exchange at global scale, Environmental
1110 Chemistry, 13, 390-412, 10.1071/EN14255, 2016.
1111
1112 von Salzen, K., Scinocca, J. F., McFarlane, N. A., Li, J. N., Cole, J. N. S., Plummer, D.,
1113 Verseghy, D., Reader, M. C., Ma, X. Y., Lazare, M., and Solheim, L.: The Canadian Fourth
1114 Generation Atmospheric Global Climate Model (CanAM4). Part I: Representation of Physical
1115 Processes, Atmosphere-Ocean, 51, 104-125, 10.1080/07055900.2012.755610, 2013.
1116
1117 White, J., Zhang, X., Welling, L., Roman, M., And Dam, H.: Latitudinal gradients in
1118 zooplankton biomass in the tropical Pacific At 140°W During The JGOFS Eqpac study - effects
1119 of El Nino, Deep-Sea Research Part II-Topical Studies in Oceanography, 42, 715-733,
1120 10.1016/0967-0645(95)00033-M, 1995.
1121
1122 Wolf-Gladrow, D., Zeebe, R., Klaas, C., Kortzinger, A., and Dickson, A.: Total alkalinity: The
1123 explicit conservative expression and its application to biogeochemical processes, Marine
1124 Chemistry, 106, 287-300, 10.1016/j.marchem.2007.01.006, 2007.
1125
1126 Zahariev, K., Christian, J., and Denman, K.: Preindustrial, historical, and fertilization simulations
1127 using a global ocean carbon model with new parameterizations of iron limitation, calcification,
1128 and N_2 fixation, Progress in Oceanography, 77, 56-82, 10.1016/j.pocean.2008.01.007, 2008.
1129
1130 Zweng, M.M., Reagan, J.R., Antonov, J.I., Locarnini, R.A., Mishonov, A.V., Boyer, T.P.,
1131 Garcia, H.E., Baranova, O.K., Johnson, D.R., Seidov, D., and Biddle, M.M.: World Ocean Atlas
1132 2013, Volume 2: Salinity. S. Levitus, Ed.; A. Mishonov, Technical Ed., NOAA Atlas NESDIS
1133 74, 39 pp., 2013.
1134